CHEMISTRY OF MATERIALS

pubs.acs.org/cm

Article

Uncovering the Influence of Ni^{2+} Doping in Lead-Halide Perovskite Nanocrystals Using Optically Detected Magnetic Resonance Spectroscopy

Yahel Barak,[‖] Itay Meir,[‖] Joanna Dehnel,[‖] Faris Horani,[‖] Daniel R. Gamelin,* Arthur Shapiro,* and Efrat Lifshitz*

Cite This: https://doi.org/10.1021/acs.chemmater.1c03822

Read Online

ACCESS | Metrics & More | Article Recommendations | Supporting Information

Downloaded via UNIV OF WASHINGTON on February 2, 2022 at 21:33:38 (UTC).
See https://pubs.acs.org/sharingguidelines for options on how to legitimately share published articles.

ABSTRACT: Magnetic doping in halide perovskite semiconductors is of timely interest in the pursuit of new optical and magnetic properties that surpass those of the existing undoped materials. Here, we report a thorough investigation of the optical and magneto-optical properties of Ni^{2+}-doped cesium lead halide perovskite with a chemical formula $CsPb(Br_{1-x}Cl_x)_3$, implementing steady-state and transient photoluminescence (PL), polarized magneto-PL, and optically detected magnetic resonance (ODMR) spectroscopies. The magneto-PL measurements revealed three PL features with different degrees of circular polarization, associated with recombination from band-edge and trapping states. The ODMR measurements probed magnetic resonance transitions of photogenerated electrons and holes with phenomenological g-factors that deviate from those of band-edge states. Simulations of the ODMR spectra suggested carriers' trapping in shallow traps with a slight anisotropic surrounding and with weak electron−hole exchange coupling. Furthermore, we observed substantial broadening of the hole resonance, due to its spin-exchange coupling with the Ni^{2+} unpaired spins. Overall, these ODMR measurements uncovered the role of the dopant in localizing photogenerated carriers by stiffening (becoming more rigid by decreasing the structural dynamics) the crystal structure and, for the first time, provide a direct observation of carrier-dopant spin exchange interactions in metal-halide perovskite nanocrystals. These results offer insight into the influence of magnetic dopants on the electronic structures of metal-halide perovskites, with a view toward emerging spin-based devices made from perovskites.

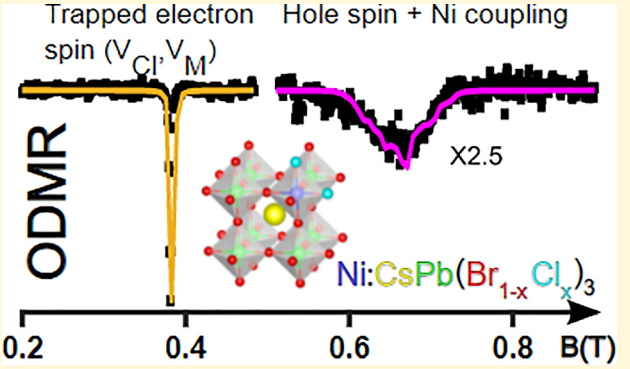

INTRODUCTION

Metal halide perovskite semiconductors have garnered intense scientific and technological interest during the past decade, triggered by their unprecedented performance in photovoltaics (PVs),[1−6] X/γ-ray detectors,[7−9] light sources, and display devices.[5,10−14] These materials are composed of metal-halide octahedrons that share corners, forming a network with voids filled by organic or atomic ions. Halide perovskites with the general chemical formula AMX_3 (e.g., A = Cs, CH_3NH_3; M = Pb, Sn; X = Cl, Br, I),[15] have been extensively studied, with properties imparting a soft nature,[16] self-healing,[17−19] tolerance to defects,[16,20−24] long carrier diffusion length,[25−28] nearly unity emission quantum yield,[16,29−31] large phonon anharmonicity,[24,32−37] strong carrier−phonon coupling, and polaron formation.[38−43]

The halide perovskites in their nanoscale forms have been a focus of scientific interest during the past decade, based on the pioneering development of colloidal synthetic procedures by Kovalenko and co-workers,[29] who stimulated preparation of different morphologies from zero- to three-dimensional structures.[44−46] Subsequently, the optical properties of perovskite materials were studied extensively.[47−56] Their photoluminescence is characterized by excitonic transitions, uniquely possessing bright triplet emission at low temperatures and dark singlet recombination at room temperature.[50,57,58] A few different magneto-optical measurements, monitoring single perovskite nanocubes[47,59] or thin films,[60−62] revealed inversion symmetry breaking in both 3D and 2D compounds, originating from an internal anisotropy caused by the composition heterogeneity, surface area, or surrounding interfaces.[63−68] The lack of inversion symmetry combined with spin−orbit coupling, as often found in these materials, leads to a Rashba

Received: November 4, 2021
Revised: January 6, 2022

© XXXX American Chemical Society

effect in both the conduction and the valence band; viz., creation of an effective internal magnetic field that splits band-edge states in k-space into two valleys, each of which accommodates photocarrier spins of opposing polarity.[47,57,62,65,69,70] The Rashba field is a source for the bright triplet recombination, as well as for spin-polarized recombination emission, with a typical lifetime of subnanoseconds.[57,58,71] These intriguing discoveries stimulated a search for the spin lifetime, spin coherence time, and values of the phenomenological g-factors.[61,72−77] Most recent studies report a low-temperature spin-relaxation time (T_1) comparable with the radiative lifetime (∼250 ps) and a spin coherence time varying from ∼4 to ∼70 ps[69,76−78] and the exceptional case of 300 ps,[77] all rivaling that of the classic III−V self-assembled quantum dots.[79,80] Besides the fast and bright excitonic emission, long emission tails of uncertain origin, up to a tenth of a nanosecond, were reported and may be related to shallow trap recombination,[52] to electron−phonon polaron formation,[41,43] or to delayed luminescence after charge separation and release.[71,81,82] Moreover, recent studies have revealed superfluorescence in self-assembled halide perovskite nanocubes, characterized by a rise of emission intensity, accelerated radiative decay, a spectral shift, and photon bunching, with respect to dispersed particles.[83,84] The observed absolute g-factors, reflecting the electronic characteristics of photogenerated carriers, were reported to vary from 2.3 to 2.6 for the electron ($|g_e|$) and 0.3 to 0.7 for the hole ($|g_h|$), with anisotropy with respect to the reference axis, but with variability in magnitude or/and sign that depends on the specific chemical composition.[74,75,77,85,86] In any event, recent explorations of spin properties in halide perovskites show promising potential for implementation in spin-based technologies such as memory and quantum computation/information.

Currently, a new area of investigation is being developed, incorporating dopant ions in halide perovskite semiconductors to engineer new optical, electronic, and magnetic properties beyond those of undoped samples. The embedding of dopant ions was accomplished either by their incorporation during the host growth[87] or as a post-treatment while using cation/anion exchange processes.[88] Both reactions can be carried out at relatively low temperatures, thus avoiding thermally activated out-diffusion of the dopants, as well as good control of their position and concentration.[87] Previous publications reported the incorporation of iso-valent as well as heterovalent ions into halide perovskite structures.[89] Heavy metals (Sn^{2+}, Sb^{3+}, and Bi^{3+})[90−97] have been incorporated to reduce toxicity in Pb^{2+}-based perovskite compounds.

The possibility of enhanced spintronic functionality has stimulated vast interest in magnetic doping of perovskites by transition metal cations such as Mn^{2+}, Co^{2+}, Ni^{2+}, and Cu^{2+},[98−118] aiming to couple the dopant spins with those of the host carriers. Surprisingly, current reports designate that magnetism of first-row transition metals stays mostly silent within halide perovskite host crystals, for reasons that are not currently understood.[119−122] Nevertheless, metal impurities could have an indirect impact on the host magneto-optical properties. In particular, first row transition metal cations possess stronger M−X chemical bonding with respect to Pb−X, according to extended X-ray absorption fine structure (EXAFS) observations.[102] Reduction in M−X lengths shrinks the octahedrons' volume and subsequently leads to reduction of the A-site cation's motion. Thus, dopants provide structural stability, but at the same time, may generate an anisotropic crystal field accompanied by electrostatic polarization that could intensify the Rashba effect.[123] Depending on the electronic band alignment between the perovskite host and dopant d-states, a host excitation energy can be transferred into the dopant d-states resulting in d−d recombination (e.g., the yellow-orange Mn d−d emission). Should be noted that d−d transitions of Ni^{2+} ions in octahedra sites fall in the infrared spectral regime and, thus, will not be monitored in the current study. Recent studies of Ni doping described the general influence of the ions on the host properties, showing significant improvement of emission quantum yields, absorption and emission spectral shifts, and extension of radiative lifetimes, with respect to the undoped hosts.[99,101−105,107,108] One study proposed that the improved quantum yield results from an outward diffusion of Pb^{2+} ions toward surfaces, followed by the formation of a PbX_2 epitaxial shell (under halide rich conditions); viz., creating passivation by a lamellar capsule via van der Waals forces.[124] The Lifshitz group recently prepared Ni-doped $CsPb(Br_{1-x}Cl_x)_3$ perovskite nanocrystals (NCs)[111] using a unique postsynthesis treatment which involved a coexchange of anion and cation and demonstrated an emission quantum yield of ∼45%, far beyond that of the parent host materials (∼7%). It is noteworthy that Cl-based perovskites show a tendency to form Cl vacancies with a direct impact on the emission quantum efficiency.[125]

Other exotic elements from the lanthanide family (Yb^{3+}, Eu^{3+}, Gd^{3+}, Ce^{3+}, Tb^{3+})[126−134] have been used as dopants, which are characterized by their atomistic f−f or f−d transitions, tunable from the blue edge of the visible to the near-infrared (NIR) spectral regimes. These dopants enhance host materials with new optical properties for display devices.[135,136] Despite wide interest in doping perovskite materials, critical knowledge regarding the dopant's effect on magneto-optical properties of $APbX_3$ halide perovskites remains elusive.

Here, we report an extensive spectroscopic investigation of Ni^{2+}-doped cesium lead halide perovskite nanocrystals (NCs) with a chemical formula $CsPb(Br_{1-x}Cl_x)_3$. To elucidate the role of the dopants, specialized spectroscopic means have been employed, including steady-state and transient (magneto) photoluminescence (PL) spectroscopies, recorded at various temperatures. Additionally, optically detected magnetic resonance (ODMR) spectroscopy has been implemented for the first time for the study of halide perovskites. The unprecedented magneto-PL measurements revealed the occurrence of three recombination events in the Ni^{2+}-doped NCs with different degrees of circular polarization (DCP), all slightly red-shifted from the band-edge energy, demonstrating obvious contrasting behavior between the undoped and doped NCs. The ODMR measurements on the doped NCs provide rich information about the recombination processes, whereas similar magnetic resonance effects were absent in the undoped NCs. The ODMR revealed spin-flip processes of both electron and hole with phenomenological g-factors deviating from those of the electronic band-edge, indicating carrier localization at shallow traps (e.g., vacancies). The magnetic resonance observations are corroborated by a theoretical spin Hamiltonian model. These results show weak spin-exchange interaction between the localized carriers and, more importantly, also indicate a spin-exchange coupling between a hole spin and Ni^{2+} unpaired electronic spins. These magnetic resonance data uncover the effect of the dopant in stiffening

https://doi.org/10.1021/acs.chemmater.1c03822
Chem. Mater. XXXX, XXX, XXX−XXX

the entire crystal, supposedly inducing metal/halide vacancies, and enabling local host−dopant spin−spin interactions which are otherwise blurred in soft perovskite undoped materials.

RESULTS AND DISCUSSION

The investigated samples included undoped $CsPb(Br_{1-x}Cl_x)_3$ and Ni^{2+}-doped $CsPb(Br_{1-x}Cl_x)_3$ perovskite NCs. Doping was accomplished via a postsynthesis coexchange of cation and anion.[111] A schematic of the Ni^{2+}-doped halide perovskite structure is shown in Figure 1a, where the various elements are

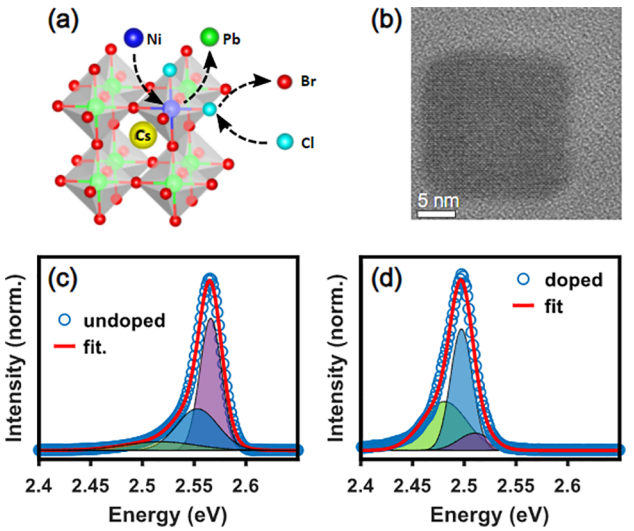

Figure 1. Structural details and optical observations: (a) Schematic structure of Ni^{2+}-doped $CsPb(Br_{1-x}Cl_x)_3$ structure. (b) HR-TEM image of a single NC. (c, d) Reflectance and photoluminescence (PL) spectra of the undoped (c) and Ni^{2+} doped (d) $CsPb(Br_{1-x}Cl_x)_3$ NCs, recorded at 4 K. E_g, Electronic band-edge energy; Gaussian best fit curves (purple, blue, and green) show the PL of the doped NCs. All data were recorded under low-power illumination (<0.5 kW/cm^2).

presented in different colors. Figure 1b represents a high-resolution transmission electron microscope image (HR-TEM) of a single NC. The cube-shaped NCs have an average size of ∼9.0 nm, possessing high crystallinity, with the chemical formula $CsPb_{0.98}Ni_{0.02}(Br_{0.49}Cl_{0.51})_3$. The composition was verified by scanning TEM along with energy dispersive elemental mapping, inductively coupled plasma atomic emission spectrometry, and X-ray photoelectron spectroscopy (XPS) as reported in ref 111. These measurements showed a slight composition variability in different batches, where the Ni^{2+} atomic percentage varied between 1.3 and 2.0%. The XPS measurements verified the integration of Ni^{2+} in the bulk position with a minor amount of Ni−O contribution at the surface (mainly related to Ni−oleic acid bonding).

Ni^{2+} is a non-Kramers ion with an integer electron spin value $S = 1$ in its ground state. A few previous studies[137,138] identified Ni^{2+} doping in various crystals (e.g., $NiBr_2$, Ni^{2+}-doped $CsMgBr_3$) using Q-band electron spin resonance (ESR) spectroscopy, which released an isotropic g-factor ∼ 2.3 and crystal field that varied between 7000 and 20 000 cm^{-1},[138] depending on the host composition. In the current study, an attempt to identify the Ni^{2+} doping site via X-band ESR spectroscopy was enabled, more likely due to its exceptionally large crystal field. However, the influence of Ni^{2+} unpaired electronic spins on other physical properties of metal halide perovskites is strongly pronounced, as elaborated below.

The optical and magneto-optical properties of the Ni^{2+}-doped $CsPb(Br_{1-x}Cl_x)_3$ NCs described above were investigated by recording PL spectra at various temperatures and in the presence of an external magnetic field (so-called magneto-PL). The data were compared with those collected for the parent compounds with the same stoichiometry of $CsPb(Br_{1-x}Cl_x)_3$. Figure 1c,d depicts PL spectra of the undoped and doped $CsPb(Br_{1-x}Cl_x)_3$ ensembles of NCs, recorded at 4 K. The PL spectra in Figure 1c,d were best-fitted by three Gaussian functions (purple, blue, and green) with energy gaps of 5−7 meV, slightly above values of a Rashba splitting for NCs of similar size,[31,47,57] hence, raising questions about their origins. Figure S1a,b in the Supporting Information (SI) displays the absorption and PL curves of the undoped and doped NCs recorded at room temperature, revealing Stokes shifts of ∼4 meV between the PL maxima and the band-edge energy, hence proposing an excitonic character to the high energy side of the band. Figure S1c depicts a set of PL spectra of randomly dispersed NCs recorded at 4K under a variable illumination power from 0.5 W/cm^2 to 35 kW/cm^2. The latter measurement reveals an energy blue shift with increased pumping intensity, attributed to suppression of a high-energy band and the appearance of a lower energy feature, which may be related to the formation of multiple excitons or a charged exciton. Note that the PL data presented in Figure 1c,d, as well as those described below, were all recorded under low-power illumination (<0.5 kW/cm^2) to ensure the formation of single photogenerated electron−hole pairs. Superfluorescence is unlikely due to these low powers and to a dispersity of individual NCs.

Figure 2a,b shows contour maps of normalized PL intensities of the ensemble of undoped $CsPb(Br_{1-x}Cl_x)_3$ NCs (a) and their Ni^{2+}-doped derivatives (b) plotted versus the temperature. The high energy side of the spectra experiences a spectral shift with increasing temperature, typical for lead-halide perovskite band-edge recombination.[139,140] The changes with temperature are accompanied by broadening of the emission bands toward lower energies due to thermally induced phonon coupling.[141,142] Also, the spectra of the undoped samples show a pronounced extra deep emission band at elevated temperatures, which is absent in the spectra of the doped derivatives. Three-dimensional plots of the temperature dependent PL measurements are shown in the SI, Figure S2. Transient PL curves of the undoped and doped NCs (from the full spectral range) plotted on a log−log scale are shown in Figure 2c,d. These curves display three distinctive regions: Single exponential decays with lifetimes between 50 ps and 250 ps (see insets) which were assigned before to neutral exciton recombination;[76,78] an exponential component identified by the simulated red line, with a lifetime of ∼15 ns at the doped and undoped NCs, where such a decay can be related to a bound or a trapped exciton or even to a long-lived trion as proposed recently;[143] and a power-law component emphasized by the green simulated line in the range above 100 ns, associated with out-diffusion of carriers toward surface sites and a consequent delayed luminescence. It is worth noting that a small power-law coefficient (α) in doped NCs reveals a minor diffusion process of carriers to the surface which avoids the quenching of the luminescence intensity. Also, the transient PL curves measured under intense pumping were dominated by a picosecond decay process and saturation of the delayed recombination. In contrast, the delayed processes were mainly pronounced under mild pumping. A measure of a

https://doi.org/10.1021/acs.chemmater.1c03822
Chem. Mater. XXXX, XXX, XXX−XXX

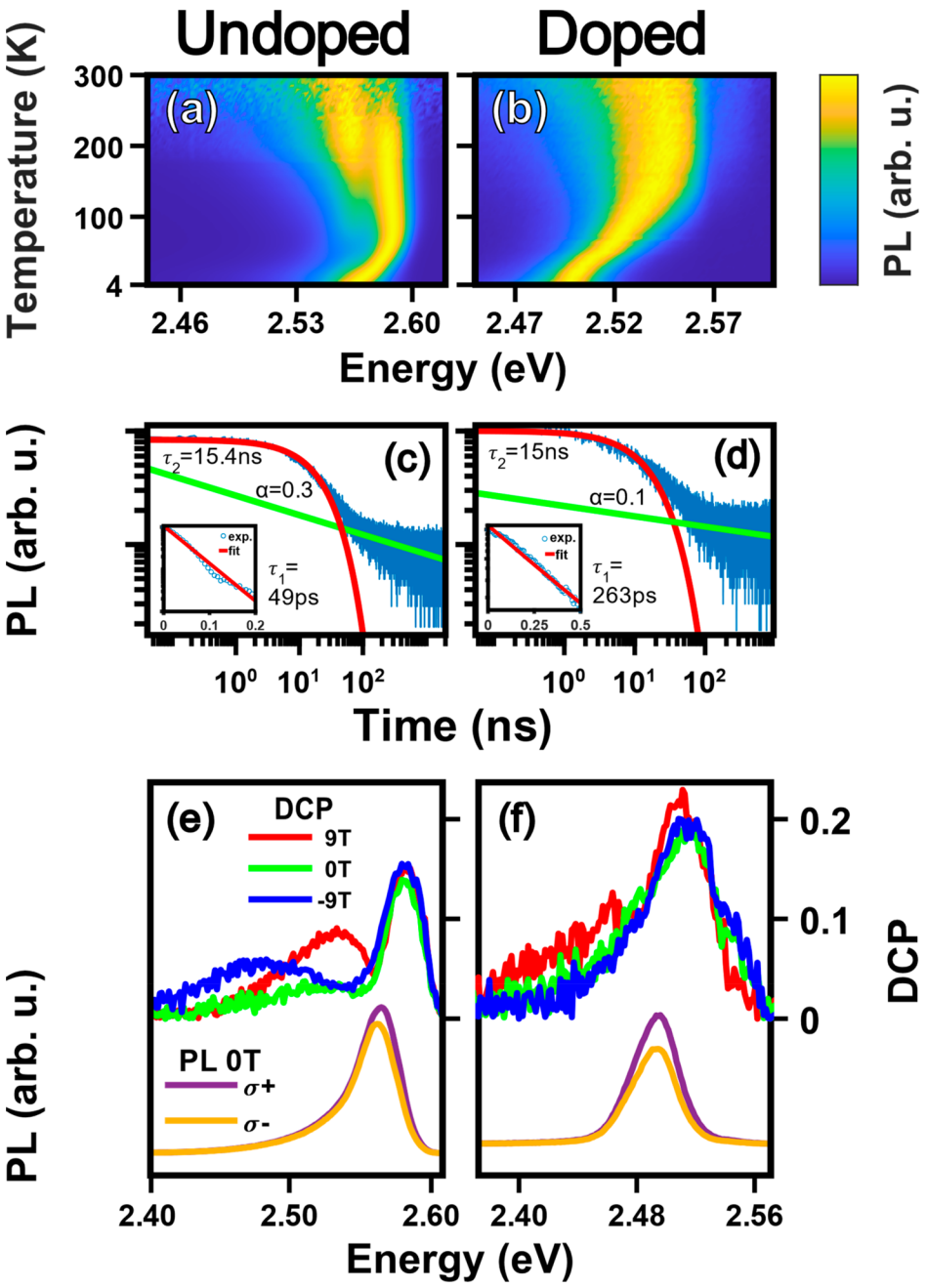

Figure 2. (a, b) Contour plots of the temperature dependence PL spectra of undoped (a) and doped (b) NCs. (c, d) Transient PL curves of the undoped (c) and doped (d) NCs (log−log presentation). The fast transient component, measured on a streak camera, is shown in the insets of the panels. (e, f) Bottom: The circularly polarized PL spectra ($\sigma\pm$), recorded at B = 0 and at 4 K for the undoped (e) and doped (f) NCs. Top: The corresponding DCP spectral trends, recorded at B = 0 and ±9 T (see legend).

component that is recognized by a power-law slow process under a mild pumping condition was further investigated, employing the ODMR technique. This method is solely limited for a measure of radiative/nonradiative processes that is compatible with or longer than the spin−lattice relaxation time (~nanoseconds)[76] for band-edge carriers in halide perovskites; however, it is expected to be substantially longer (~hundreds of microseconds) for localized carriers at trapping sites.[144]

Figure 2e,f, bottom curves, illustrate the circularly polarized PL spectra ($\sigma\pm$) of undoped (e) and doped (f) NCs, monitored in the absence of an external magnetic field (B = 0) at 4 K. Note, the polarized PL spectra relate to NCs which were dispersed onto a Si substrate with partial self-assembly, in contrast to the measurements shown in Figure 2a−d. The top curves in Figure 2e,f present three trends (recorded at B = 0 and ±9 T) of the degree of circular polarization, which is defined as DCP = $(I_{\sigma^+} - I_{\sigma^-})/(I_{\sigma^+} + I_{\sigma^-})$, when $I_{\sigma\pm}$ is the emission intensity at the indicated polarization. Complementary DCP plots recorded over the range of $-9 < B < 9$ T are shown in the SI, Figure S4. A careful examination of the DCP plots reveals interesting trends: (i) The circularly polarized bands of the doped NCs experience a slight energy shift with respect to the corresponding undoped ones. (ii) The DCP trends offer a merit beyond that of the PL raw data, by resolving a few different recombination events. A careful

https://doi.org/10.1021/acs.chemmater.1c03822
Chem. Mater. XXXX, XXX, XXX−XXX

examination of the DCP plots reveals interesting trends. (iii) The DCP curves of the doped sample expose three main spectral regions: the two highest energy features (2.54 eV, 2.50 eV) refer to the two opposed polarized triplet exciton components (e.g., Rashba split), while the low energy feature (2.35−2.45 eV) may refer to recombination at a trapping site. (iv) The triplet exciton components (2.58 eV) are degenerate in the DCP of the undoped sample. (v) Two different deep emission processes with opposing polarities are pronounced in the undoped sample (2.45 and 2.53 eV), when the lowest energy one is absent in the doped sample. Interestingly, the magneto-PL spectra were found also to be linearly polarized (~33%) at a zero external magnetic field (SI, Figure S3); nevertheless, this polarization diminished gradually upon the increase of the magnetic field. Linearly polarized PL has been identified as a signature of a weak Rashba splitting in previous studies of lead-halide perovskites performed close to a zero magnetic field,[47,49,57] due to a mixing of close lying triplet and singlet states with a small spread across ~1−2 meV. The larger interspread gained at the highest magnetic field exposes the circular polarization of individual triplet states.

Optically detected magnetic resonance (ODMR) spectroscopy has been implemented to further understand long-lived magneto-optical properties in the studied NCs. An ODMR experiment measures a differential change in the luminescence intensity ($\Delta I/I$, where I = PL intensity) due to a magnetic resonance effect in the excited state, versus the strength of an external magnetic field. For such an experiment, the sample was placed within a microwave (MW) cavity operating as an antenna at a fixed frequency of ~10.78 GHz, and the cavity was mounted into a magneto-optical cryostat. All reported data were measured at 2.17 K. The emission has been monitored either parallel (Faraday) or in the normal direction (Voigt) with respect to that of the magnetic field. Furthermore, the MW radiation was modulated with variable audio frequencies from 100 Hz to ~10 000 Hz. This modulation enables lock-in detection of the differential luminescence intensity and furthermore had a substantial influence on the ODMR spectral pattern itself. Further details about the ODMR setup are given in the Methods section.

Notably, whereas the Ni^{2+}-doped perovskite NCs show rich ODMR spectra, the corresponding undoped NCs solely stayed silent regarding magnetic resonance transitions (viz., absence of any ODMR spectrum). The appearance of the ODMR signal in the doped sample can be explained by stabilization of the crystal skeleton by the stronger bonding between Ni−Br and Ni−Cl with respect to Pb-based bonds. Accordingly, the following sections exposed in detail the ODMR spectra of the Ni-doped $CsPb(Br_{1-x}Cl_x)_3$ NCs, while monitoring different spectral windows of their PL spectrum.

Figure 3a depicts an ODMR spectrum monitoring the entire emission as in Figure 1d, recorded at 4 K with a Voigt alignment ($B\perp$ excitation beam). The spectrum is dominated by a sharp, intense negative resonance centered around 0.383 T and another weak and broad negative resonance around 0.67 T. The red curve in Figure 3a shows a simulated spectrum generated using a spin-Hamiltonian, revealing average g-factors of 2.01 for the low field resonance and 1.15 for high resonance band, both of which deviate from those of band-edge carriers ($|g_e|$: 2.3 to 2.6; $|g_h|$: 0.3 to 0.6).[61,72−77] These differences reflect the involvement of environmental distortions and/or localization of the photogenerated carriers. Details of the spin-Hamiltonian simulations are elaborated in the text below.

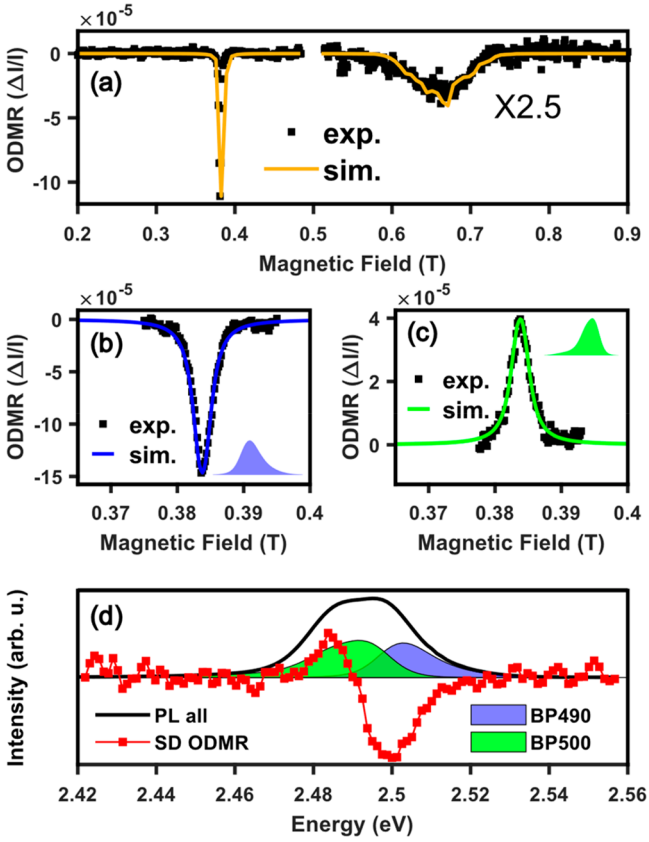

Figure 3. ODMR spectra of Ni^{2+} doped $CsPb(Br_{1-x}Cl_x)_3$NCs: (a, b, c) The ODMR spectra recorded under Voigt configuration at 2.17 K when monitoring: the full PL spectral range (a), the blue region (b), and the green region (c) from the PL band (see Figure 1d). The experimental raw data are shown by the black symbols and the theoretical simulations by the colored curves. (d) The spectral dependence ODMR (red line) spectrum is displayed in comparison with the PL spectrum (black line). The corresponding blue and green PL spectral regions refer to spectral scans with 490 or 500 nm centered band-pass filters, respectively.

The black symbols in Figure 3b depict an ODMR spectrum of doped NCs, monitored at the blue spectral window of the PL band. This spectrum was recorded in-phase (IP) with the MW pulse, which was chopped at an audio frequency of ~180 Hz under Voigt optical alignment. The blue line corresponds to a theoretical simulation. Similar spectra recorded with the same MW conditions but optically monitored along the Faraday direction ($B\|$ excitation beam) and through circular polarizers ($\sigma\pm$) are shown in the SI, Figure S5. The polarized spectra illustrate a pattern compatible with that shown in Figure 3b, suggesting that the Voigt spectrum consists of the sum of the two circular polarized components. Based on this interpretation, the following discussion focuses on the ODMR observations obtained under the Voigt alignment which offers the largest signal/noise ratio.

Figure 3c displays an ODMR spectrum recorded in the Voigt configuration while monitoring the green spectral window of the PL band. The spectrum comprises a positive resonance. The opposing signs in the ODMR spectra of the blue and green spectral windows indicate dissimilar recombination mechanisms, although the resonance extrema possess a very similar g-factor value around $g \sim 2.00$ and suggest an

https://doi.org/10.1021/acs.chemmater.1c03822
Chem. Mater. XXXX, XXX, XXX−XXX

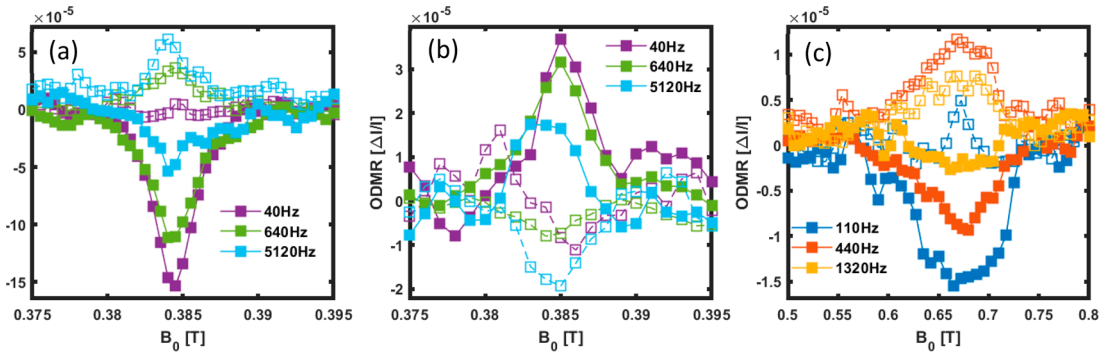

Figure 4. Influence of MW audio modulation frequency on the ODMR spectral patterning: ODMR spectra measured under various audio frequencies when monitoring: the blue spectral region (a), the green spectral region (b), and the full PL spectral window (selectively at the far-field resonance) (c). The solid (open) symbols correspond to a measure of the luminescence in-phase (out of phase) with respect to the rising edge of the MW pulse.

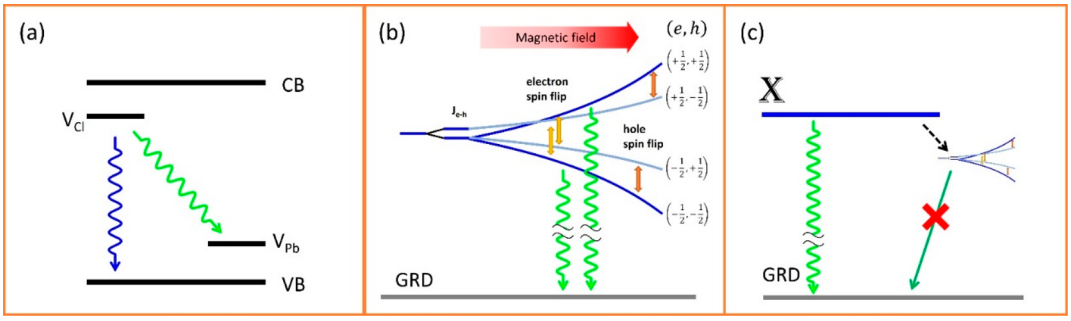

Figure 5. Scheme of optical and spin manifolds related to the following: (a) Proposed recombination routes associated with the green and blue emission bands, involving shallow traps at V_{Cl} and V_{Pb} sites and a single electronic band-edge. (b) Trap-to-band or trap-to-trap recombination involving an electron and hole pair in turn with S_e and S_h spin momentum, with a weak mutual spin exchange interaction (J_{e-h}). The wavy arrows designate radiative recombination. Spin flip of an electron or a hole is marked by the yellow and orange arrows, respectively. (c) Similar spin manifold to that in (a) which is populated via intersystem crossing and the consequence differential change in the exciton emission (see marked by the wavy arrow) comprises the ODMR signal.

involvement of a common electronic state in the recombination processes.

Figure 3d shows the spectral dependence of the ODMR (SD-ODMR), plotted by red symbols, in comparison with the low temperature PL spectrum (black curve) of the doped NCs. The blue and green shades refer to spectral scans of the PL band while using 490 or 500 nm band-pass filters, respectively, thus isolating the lowest DCP components in the PL and the MPL spectra (see Figures 1d and 2f).

The SD-ODMR curve is associated with a scan of the PL spectrum under continuous magnetic resonance conditions (i.e., MW radiation of ∼10.78 GHz and a magnetic field of 0.38 T). The figure shows that the SD-ODMR curve tends toward negative values at the blue side of the spectrum and switches to a positive response in the green spectral region. This behavior confirms the opposing signs seen in Figure 3b,c. The change in the sign of an ODMR signal is explained below, by a differentiation between a thermalized (depletion) and unthermalized (enhancement) behavior, mainly dictated by the ratio between a radiative time (τ_R) and the spin relaxation time (T_1).[145]

Beyond the steady-state ODMR measurements, temporal information was deduced from inspecting changes in the ODMR pattern upon variation of the audio-modulation frequency of the MW. Figure 4a,b presents the ODMR spectra of the blue (a) and green (b) spectral windows recorded under variable MW audio frequencies, in-phase (IP, solid symbols) and out-of-phase (OP, open symbols) with respect to the MW pulses. This set of spectra brings to light a few interesting facts: (i) The OP signals imply events occurring in the dwell times between adjacent MW pulses (e.g., spin relaxation). (ii) The IP signals reflect the radiative relaxation during the MW pulse. The audio frequency in which the OP component nearly vanishes provides an upper limit to the spin relaxation time, thus revealing a spin−lattice relaxation of T_1 = 0.2 ms for an electron involved in the blue and green emission processes. Figure 4c plots the frequency dependence of the high-field ODMR resonance (as shown in Figure 3a), from which hole-spin relaxation of T_1 = 0.75 ms was deduced, obviously differing from that found for an electron spin. Furthermore, the hole spin experiences exchange coupling with the Ni^{2+} dopant spins, and that fact persuades an extension of its spin-relaxation time.

The ODMR spectra shown in Figures 2 and 3 were simulated using the following spin-Hamiltonian:

$$H_s = \mu_B \vec{J}_{e(t)} \overline{\overline{g}}_{e(t)} \vec{B}_0 + \mu_B \vec{S}_{h(t)} \overline{\overline{g}}_{h(t)} \vec{B}_0 + \mu_B \vec{S}_{Ni} \overline{\overline{g}}_{Ni} \vec{B}_0 + J_{e(t)-h(t)} \vec{J}_{e(t)} \vec{S}_{h(t)} + J_{h(t)-Ni} \vec{S}_{h(t)} \vec{S}_{Ni} \quad (1)$$

The first three terms in eq 1 correspond to the Zeeman interactions of a free or trapped electron/hole ($J_{e,h(t)}$, t = trap), a hole ($S_{h(t)}$), and the Ni^{2+} dopant (S_{Ni}). The fourth and fifth terms are associated with the electron−hole (J_{e-h}) and hole−dopant ($J_{h(t)-Ni}$)[57,146,147] spin exchange coupling, respectively. As a preliminary assumption, the hyperfine interactions

https://doi.org/10.1021/acs.chemmater.1c03822
Chem. Mater. XXXX, XXX, XXX−XXX

Table 1. Parameters Used for the ODMR Simulations (Based on the Spin Hamiltonian in Equation 1)

	g_e^z	g_e^{xy}	g_h^z	$g_h^{x,y}$	$g_{Ni}^{x,y,z}$	J_{e-h} (μeV) (ΔJ_{e-h}, μeV)[a]	J_{h-Ni} (μeV) (ΔJ_{h-Ni}, μeV)[a]
full spectral range	1.99	1.99	1.12	1.14	2.3[b]	0.10 (0.05)	2 (1)
blue component	1.994	1.994	1.12	1.14	2.3	0.10 (0.05)	-
green component	2.01	2.01	1.12	1.14	2.3	0.10 (0.05)	-

[a]A Gaussian distribution of J values. [b]Reference 138.

involving abundant spin-bearing isotopes from dopants or resident atoms were neglected, and a justification is further elaborated below. Also, the nonlinearity of a Zeeman-like term owed to a contribution of a Rashba field was excluded from the simulation, due to a focus in the ODMR study on sub-band gap transitions rather than band-edge luminescence.

Figure 5a illustrates the proposed optical transition correlated with the ODMR observations, comprised of an electron at a donor site (e.g., V_{Cl^-}) and a hole either at a band-edge or at an acceptor site (e.g., $V_{Pb^{2+}}$). The corresponding magnetic resonance transitions are illustrated schematically in Figure 5b, showing a spin manifold under the presence of a magnetic field. The diagram describes an electron−hole pair in the excited state, where each individual carrier possesses a spin-moment of $S = 1/2$ ($m_S = \pm 1/2$), hence generating a total pair momentum of $S_{e-h} = 1, 0$ ($m_S = \pm 1$, 0 and $m_S = 0$, respectively). The relative energies of these states at $B_0 = 0$ depend on the electron−hole exchange splitting (J_{e-h}) and the surrounding anisotropy. Note that, in the case of halide perovskites, individual carriers with $S = 1/2$ are associated with band-edge states,[47,49,148,149] but such a moment is also retained upon localization or trapping of one or both of those carriers. The bright radiative relaxation processes from triplet states ($m_S = \pm 1$ components) are indicated by the wavy arrows. The magnetic resonance transitions (e.g., spin-flip of an electron or/and a hole) are indicated by the orange/yellow arrows. Upon nonresonant excitation and in the case of fast recombination (short τ_R), the increase of population of a radiative state (with $m_S = \pm 1$) by the magnetic resonance transition leads to an enhanced luminescence differential (viz., to a positive ODMR signal). In contrast, a slow recombination process (e.g., band-to-trap, trap-to-trap, or delayed luminescence) with τ_R longer than the value of T_1 would allow population thermalization within the spin manifold and would consequently generate a negative ODMR signal. Significantly, a negative resonance can also appear when the entire manifold is related to a nonradiative trapped center; however, the luminescence is monitored in resonance with a band-edge transition, as illustrated schematically in Figure 5c. Indeed, Figure 3a,b displayed dominancy of negative signals, related to either one of the cases shown in Figure 5b,c.[144,145,150]

Spin Hamiltonian simulations were carried out based on the spin manifold shown in Figure 5b. The magnetic parameters deduced from simulating the ODMR spectra in Figures 3 and 4 are summarized in Table 1, and the simulated spectra are shown next to the experimental data in Figure 2a−c. The resonance at low magnetic field in Figure 3a is associated with an electron spin-flip with a mean g_e value of 1.998. The high-field signal is associated with a hole spin-flip with a g_h value of 1.12, meaning that the carrier feels spin−orbit interaction and anisotropy in the chemical surrounding. Importantly, the hole resonance is much broader than the electron resonance, despite observations that electrons in perovskites have much shorter spin coherence times (T_2), as revealed from the time-resolved Faraday rotation measurements.[77] Simulation of this excess broadening of the high-field resonance required the introduction of exchange coupling between Ni^{2+} spins ($S = 1$) and the perovskite hole, parametrized in eq 1 by ($J_{h(t)-Ni}$). The fine structure anticipated for this resonance is weakly resolved due to its low intensity and presumed inhomogeneous broadening. Simulations illustrating the high-field resonance dependence on ($J_{h(t)-Ni}$) are shown in the SI, Figures S6 and S7, confirming a substantially narrower band in the absence of h−Ni^{2+} coupling, and best fit upon the consideration of such a coupling with a magnitude of $J_{h-Ni} = 2$ μeV with width of 1 μeV. These results demonstrate that although magnetic resonance transitions within Ni^{2+} stay silent, the dopant's unpaired spins are indeed coupled to a spin of a photogenerated carrier, with a preference for interaction with a hole spin, due to a contribution of p-orbits of the halides. The value of g_h deviates from that of a band-edge carrier and also from the value of a free carrier, owing to the surplus h−Ni^{2+} exchange.

The value of J_{e-h} deduced from the ODMR simulations is relatively small ($\sim\mu$eV) compared to those reported for excitons in perovskites, reflecting a relatively weak electron−hole interaction and corroborating the interpretation that each carrier experienced a localization at a different crystallographic site. Although the halide perovskites are known for their defect tolerance, this does not exclude the existence of trapping centers, which might be associated with self-trapping after excitation,[151−155] a trapping at above band gap states, or shallow in-gap states. In addition, in recent studies, the source of a long recombination time has been associated with an Auger process that involves carrier trapping at a defect surface site.[156] Thus, whether a photogenerated carrier diffuses directly or is first ejected by an Auger process to a remote state and is then trapped, it is sustained for some time before recombination with a counter charge. Meanwhile, the ODMR experiment can be detected following either one of the routes displayed in Figure 5. A few options have been proposed theoretically as shallow trapping states,[124] mostly related to vacancies at metal or halide sites in close proximity to the exterior NC surfaces. Note that the preparation of Ni^{2+}-doped NCs was accompanied by anion exchange of about 50% of Br for Cl. A chloride agent was used in Ni^{2+} doping to assist uniform exchange with Pb^{2+} ions that resulted in a stronger M−X bond. However, the combined cation/anion exchange process may create vacancies, with a well-known tendency for chloride vacancies.[157] Antisite defects including M^{2+} in the Cs^+ site can be excluded, as those are predicted to generate deep traps,[157] but our data show only minor Stokes shifts of ∼4−7 meV from the absorption edge. Furthermore, previous DFT calculations (ref 111) have indicated an energetic preference for Ni^{2+} to exchange for Pb^{2+} ions at the lattice B site. Based on these considerations, the blue- and green-emission components are associated either with trap-to-band or with trap-to-trap recombination, where $V_{Pb^{2+}}$ is considered a likely acceptor and V_{Cl^-} is considered a potential donor (see scheme in Figure 5a). At last, a preliminary assumption was made earlier,

https://doi.org/10.1021/acs.chemmater.1c03822
Chem. Mater. XXXX, XXX, XXX−XXX

neglecting hyperfine interactions emanating from neutral abundance isotopes of a Ni^{2+} or host elements (Pb, Br). The Ni^{2+} hyperfine constant is ~0.1 μeV,[158] while that of Pb^{2+} was recently evaluated to be ~20 μeV in relation with a band-edge hole.[75] The hyperfine of Ni^{2+} is negligible with respect to the J_{h-Ni} exchange, while that of Pb^{2+} normally induces a giant broadening, which is obviously absent in our case. Furthermore, most monitored carriers by the ODMR method were localized at a trapping site, without an efficient overlap with Pb^{2+} nuclei. Thus, the simulations illustrated in Figures S6 and S7 gain a high conformity in exposing the h−Ni electron spin exchange coupling.

SUMMARY

The current work has examined the effect of dilute Ni^{2+} doping on the photophysics of $CsPb(Br_{1-x}Cl_x)_3$ NCs (nanocubes) with an average size of ~9 nm. The study implemented multiple different spectroscopic methods to follow changes in the (magneto-)optical properties of the halide perovskites induced by doping. A combination of variable-temperature photoluminescence (PL), transient PL, and circularly polarized PL spectroscopies exposed the presence of three distinct near-band-edge components in the NC PL spectrum, one having an extremely fast radiative lifetime (~picoseconds) and two others with nanosecond decay times. All three show circular polarization. The extended lifetime processes were correlated with delayed luminescence as justified above and are most likely associated with localized or trapped carriers induced by stiffening of the entire perovskite structure by the presence of dopants. ODMR spectroscopy confirmed the existence of carrier trapping, as deduced from the phenomenological g-factors and the spectra patterns. Above all, the ODMR data also revealed direct evidence of magnetic-exchange coupling between the Ni^{2+} unpaired spins and the spin of a hole carrier, with an extended spin-relaxation time (T_1 < milliseconds). Carrier-dopant spin exchange coupling has not been measured previously, but such coupling is of paramount importance for practical application of diluted magnetic perovskites in spin-based devices.

METHODS

Sample Preparation. Pristine $CsPbBr_3$ and Ni^{2+}-doped $CdPb(Br_{1-x}Cl_x)_3$ NCs were prepared following the procedures discussed in ref 111. The incorporation of Ni^{2+} was done in a post-treatment process, involving the coexchange of cation and anion, starting from the $NiCl_2$ precursor. The coexchange assisted in introducing the Ni cation into the heart of the nanocrystal. The uniform spread of the dopant atoms across the crystal was approved by scanning TEM combined with EDX spectroscopy (see ref 111).

Optical and Magneto-Optical Spectroscopy. The photoluminescence (PL) spectra recorded at various temperatures and the magneto-PL and the transient-PL curves were measured by mounting an ensemble of NCs (drop-casted onto a Si substrate) into a fiber-based confocal microscope. The microscope was embedded into a cryogenic system (attoDRY1000 closed cycle cryostat). The microscope included a focal lens with NA of 0.65 and a 473 nm long-pass dichroic mirror. The target sample was excited using a continuous-wave unpolarized 405 nm laser diode, and emission was detected using a FERGIE spectrograph. The transient PL curves were recorded using a pulse laser with a peak energy at 450 nm and a pulse length of 70 ps. The fast transient PL was measured via an Optronis streak camera with a repetition rate of 0.3/0.5 MHz and a scan speed of 250 ps/mm with laser pulse energy of 2 mJ/cm^2. The slow transient PL was measured with an MPD single photon avalanche diode connected to a PicoHarp300 time-correlated single photon counter (TCSP) using very low laser pulse energy of 203−510 nJ/cm^2. Magneto- and temperature-dependent PL spectra were recorded under illumination power between 254−509 W/cm^2, ensuring creation of a single electron−hole pair at the excited state (exciton or trapped carriers).

PL Decay Fitting. The exponential decay component was fitted to the equation $A\exp(-t/\tau)$ for each decay component. A is the amplitude, t is the time, and τ is the mean lifetime in which the intensity reduced to $1/e$ of its starting value A. The power law component was fitted to $f(t) = t^{-\alpha}$ by linear fitting of the logarithm of the measured intensity ($f(x) = \log(f(t))$) and the logarithm of t ($x = \log(t)$) to $f(x) = mx + b$.

ODMR Spectroscopy. In the ODMR experiment, a sample was mounted into a custom-made microwave (MW) cavity operating at the x-band frequency (~10.7 GHz), when the end is positioned at the center of a superconducting magnet (split Helmholtz coil). All parts mentioned were immersed in a liquid helium cryostat, operating at a superfluid helium temperature (2.17 K). The sample was excited by a continuous-wave diode laser at 405 nm. The MW signal was generated by a MW generator, while the power output was modulated via a square-wave generator, with audio-frequencies ranging from 40 Hz to 5 kHz. The PL emission was monitored by a Si photodiode and was fed into a lock-in amplifier. The lock-in detection was synchronized with the MW modulation frequency, monitoring either in-phase (IP) or out-of-phase (OP) with respect to the rising edge of the MW pulse.

ASSOCIATED CONTENT

Supporting Information

The Supporting Information is available free of charge at https://pubs.acs.org/doi/10.1021/acs.chemmater.1c03822.

Absorption and photoluminescence (PL) spectra of undoped and doped derivatives at room temperature; PL spectra of dispersed doped perovskite nanocubes measured under different excitation powers; 3D plots of temperature dependent PL spectra of undoped and doped samples; linear polarized spectrum of Ni^{2+} doped perovskite nanocubes; and steady-state ODMR spectra of doped perovskite nanocubes monitored under Faraday optical alignment with circular polarizers (PDF)

AUTHOR INFORMATION

Corresponding Authors

Daniel R. Gamelin − *Department of Chemistry and the Molecular Engineering Materials Center, University of Washington, Seattle, Washington 98195-1700, United States;* orcid.org/0000-0003-2888-9916; Email: gamelin@uw.edu

Arthur Shapiro − *Schulich Faculty of Chemistry, Solid State Institute and the Hellen Diller Center, Russell Burry Nanotechnology Institute, Grand Technion Energy Program, Technion−Israel Institute of Technology, Haifa 3200003, Israel; Optical Materials Engineering Laboratory, Department of Mechanical and Process Engineering, ETH Zurich, 8092 Zurich, Switzerland*; Email: shapiroa@ethz.ch

Efrat Lifshitz − *Schulich Faculty of Chemistry, Solid State Institute and the Hellen Diller Center, Russell Burry Nanotechnology Institute, Grand Technion Energy Program, Technion−Israel Institute of Technology, Haifa 3200003, Israel;* orcid.org/0000-0001-7387-7821; Email: ssefrat@technion.ac.il

https://doi.org/10.1021/acs.chemmater.1c03822
Chem. Mater. XXXX, XXX, XXX−XXX

Authors

Yahel Barak − *Schulich Faculty of Chemistry, Solid State Institute and the Hellen Diller Center, Russell Burry Nanotechnology Institute, Grand Technion Energy Program, Technion−Israel Institute of Technology, Haifa 3200003, Israel*

Itay Meir − *Schulich Faculty of Chemistry, Solid State Institute and the Hellen Diller Center, Russell Burry Nanotechnology Institute, Grand Technion Energy Program, Technion−Israel Institute of Technology, Haifa 3200003, Israel*

Joanna Dehnel − *Schulich Faculty of Chemistry, Solid State Institute and the Hellen Diller Center, Russell Burry Nanotechnology Institute, Grand Technion Energy Program, Technion−Israel Institute of Technology, Haifa 3200003, Israel*

Faris Horani − *Schulich Faculty of Chemistry, Solid State Institute and the Hellen Diller Center, Russell Burry Nanotechnology Institute, Grand Technion Energy Program, Technion−Israel Institute of Technology, Haifa 3200003, Israel*

Complete contact information is available at: https://pubs.acs.org/10.1021/acs.chemmater.1c03822

Author Contributions

[‖](Y.B., I.M., J.D., and F.H.) Equal contribution.

Notes

The authors declare no competing financial interest.

■ ACKNOWLEDGMENTS

The authors acknowledge the financial support from the Neubauer Family Foundation, Israel Science Foundation (No. 2528/19 and No. 1045/17), the USA/Israel Binational Science Foundation (No. 2016156 and No. 2020076), and the joint USA National Science Foundation−USA/Israel Binational Science Foundation (NSF-BSF, No. 2017637). Additional support from the UW Molecular Engineering Materials Center (DMR 1719797 to D.R.G.), an NSF Materials Research Science and Engineering Center, is gratefully acknowledged.

■ REFERENCES

(1) Lee, M. M.; Teuscher, J.; Miyasaka, T.; Murakami, T. N.; Snaith, H. J. Efficient Hybrid Solar Cells Based on Meso-Superstructured Organometal Halide Perovskites. *Science (80-.).* **2012**, *338* (6107), 643−647.

(2) Kojima, A.; Teshima, K.; Shirai, Y.; Miyasaka, T. Organometal Halide Perovskites as Visible-Light Sensitizers for Photovoltaic Cells. *J. Am. Chem. Soc.* **2009**, *131* (17), 6050−6051.

(3) Etgar, L.; Gao, P.; Xue, Z.; Peng, Q.; Chandiran, A. K.; Liu, B.; Nazeeruddin, M. K.; Grätzel, M. Mesoscopic CH3NH3PbI3/TiO2 Heterojunction Solar Cells. *J. Am. Chem. Soc.* **2012**, *134* (42), 17396−17399.

(4) Kazim, S.; Nazeeruddin, M. K.; Grätzel, M.; Ahmad, S. Perovskite as Light Harvester: A Game Changer in Photovoltaics. *Angew. Chemie - Int. Ed.* **2014**, *53* (11), 2812−2824.

(5) Stranks, S. D.; Snaith, H. J. Metal-Halide Perovskites for Photovoltaic and Light-Emitting Devices. *Nat. Nanotechnol.* **2015**, *10* (5), 391−402.

(6) Christians, J. A.; Fung, R. C. M.; Kamat, P. V. An Inorganic Hole Conductor for Organo-Lead Halide Perovskite Solar Cells. Improved Hole Conductivity with Copper Iodide. *J. Am. Chem. Soc.* **2014**, *136* (2), 758−764.

(7) Yakunin, S.; Dirin, D. N.; Shynkarenko, Y.; Morad, V.; Cherniukh, I.; Nazarenko, O.; Kreil, D.; Nauser, T.; Kovalenko, M. V. Detection of Gamma Photons Using Solution-Grown Single Crystals of Hybrid Lead Halide Perovskites. *Nat. Photonics* **2016**, *10* (9), 585−589.

(8) Yakunin, S.; Sytnyk, M.; Kriegner, D.; Shrestha, S.; Richter, M.; Matt, G. J.; Azimi, H.; Brabec, C. J.; Stangl, J.; Kovalenko, M. V.; et al. Detection of X-Ray Photons by Solution-Processed Lead Halide Perovskites. *Nat. Photonics* **2015**, *9* (7), 444−449.

(9) Wei, H.; Fang, Y.; Mulligan, P.; Chuirazzi, W.; Fang, H. H.; Wang, C.; Ecker, B. R.; Gao, Y.; Loi, M. A.; Cao, L.; et al. Sensitive X-Ray Detectors Made of Methylammonium Lead Tribromide Perovskite Single Crystals. *Nat. Photonics* **2016**, *10* (5), 333−339.

(10) Yan, F.; Demir, H. V. LEDs Using Halide Perovskite Nanocrystal Emitters. *Nanoscale* **2019**, *11*, 11402−11412.

(11) Yakunin, S.; Protesescu, L.; Krieg, F.; Bodnarchuk, M. I.; Nedelcu, G.; Humer, M.; De Luca, G.; Fiebig, M.; Heiss, W.; Kovalenko, M. V. Low-Threshold Amplified Spontaneous Emission and Lasing from Colloidal Nanocrystals of Caesium Lead Halide Perovskites. *Nat. Commun.* **2015**, *6*, 8056.

(12) Zhang, X.; Lin, H.; Huang, H.; Reckmeier, C.; Zhang, Y.; Choy, W. C. H.; Rogach, A. L. Enhancing the Brightness of Cesium Lead Halide Perovskite Nanocrystal Based Green Light-Emitting Devices through the Interface Engineering with Perfluorinated Ionomer. *Nano Lett.* **2016**, *16* (2), 1415−1420.

(13) Li, G.; Tan, Z. K.; Di, D.; Lai, M. L.; Jiang, L.; Lim, J. H. W.; Friend, R. H.; Greenham, N. C. Efficient Light-Emitting Diodes Based on Nanocrystalline Perovskite in a Dielectric Polymer Matrix. *Nano Lett.* **2015**, *15* (4), 2640−2644.

(14) Yan, F.; Tan, S. T.; Li, X.; Demir, H. V. Light Generation in Lead Halide Perovskite Nanocrystals: LEDs, Color Converters, Lasers, and Other Applications. *Small* **2019**, *15*, 1902079.

(15) Kieslich, G.; Goodwin, A. L. The Same and Not the Same: Molecular Perovskites and Their Solid-State Analogues. *Mater. Horizons* **2017**, *4*, 362−366.

(16) Akkerman, Q. A.; Rainò, G.; Kovalenko, M. V.; Manna, L. Genesis, Challenges and Opportunities for Colloidal Lead Halide Perovskite Nanocrystals. *Nat. Mater.* **2018**, *17* (5), 394−405.

(17) Ceratti, D. R.; Rakita, Y.; Cremonesi, L.; Tenne, R.; Kalchenko, V.; Elbaum, M.; Oron, D.; Potenza, M. A. C.; Hodes, G.; Cahen, D. Self-Healing Inside APbBr3 Halide Perovskite Crystals. *Adv. Mater.* **2018**, *30*, 1706273.

(18) Cahen, D.; Lubomirsky, I. Self-Repairing Energy Materials: Sine qua Non for a Sustainable Future. *Acc. Chem. Res.* **2017**, *50* (3), 573−576.

(19) Yadav, P.; Prochowicz, D.; Alharbi, E. A.; Zakeeruddin, S. M.; Grätzel, M. Intrinsic and Interfacial Kinetics of Perovskite Solar Cells under Photo and Bias-Induced Degradation and Recovery. *J. Mater. Chem. C* **2017**, *5* (31), 7799−7805.

(20) Kang, J.; Wang, L. W. High Defect Tolerance in Lead Halide Perovskite CsPbBr3. *J. Phys. Chem. Lett.* **2017**, *8* (2), 489−493.

(21) Huang, H.; Bodnarchuk, M. I.; Kershaw, S. V.; Kovalenko, M. V.; Rogach, A. L. Lead Halide Perovskite Nanocrystals in the Research Spotlight: Stability and Defect Tolerance. *ACS Energy Lett.* **2017**, *2* (9), 2071−2083.

(22) Brandt, R. E.; Poindexter, J. R.; Gorai, P.; Kurchin, R. C.; Hoye, R. L. Z.; Nienhaus, L.; Wilson, M. W. B.; Polizzotti, J. A.; Sereika, R.; Žaltauskas, R.; et al. Searching for "Defect-Tolerant" Photovoltaic Materials: Combined Theoretical and Experimental Screening. *Chem. Mater.* **2017**, *29* (11), 4667−4674.

(23) Meggiolaro, D.; Motti, S. G.; Mosconi, E.; Barker, A. J.; Ball, J.; Andrea Riccardo Perini, C.; Deschler, F.; Petrozza, A.; De Angelis, F. Iodine Chemistry Determines the Defect Tolerance of Lead-Halide Perovskites. *Energy Environ. Sci.* **2018**, *11* (3), 702−713.

(24) Cohen, A. V.; Egger, D. A.; Rappe, A. M.; Kronik, L. Breakdown of the Static Picture of Defect Energetics in Halide Perovskites: The Case of the Br Vacancy in CsPbBr3. *J. Phys. Chem. Lett.* **2019**, *10* (16), 4490−4498.

(25) Du, M. H. Efficient Carrier Transport in Halide Perovskites: Theoretical Perspectives. *J. Mater. Chem. A* **2014**, *2* (24), 9091−9098.

(26) Stranks, S. D.; Eperon, G. E.; Grancini, G.; Menelaou, C.; Alcocer, M. J. P.; Leijtens, T.; Herz, L. M.; Petrozza, A.; Snaith, H. J.

Electron-Hole Diffusion Lengths Exceeding 1 Micrometer in an Organometal Trihalide Perovskite Absorber. *Science (80-.).* **2013**, *342* (6156), 341−344.
(27) Zhumekenov, A. A.; Saidaminov, M. I.; Haque, M. A.; Alarousu, E.; Sarmah, S. P.; Murali, B.; Dursun, I.; Miao, X. H.; Abdelhady, A. L.; Wu, T.; et al. Formamidinium Lead Halide Perovskite Crystals with Unprecedented Long Carrier Dynamics and Diffusion Length. *ACS Energy Lett.* **2016**, *1* (1), 32−37.
(28) Zhao, Y.; Nardes, A. M.; Zhu, K. Solid-State Mesostructured Perovskite CH3NH3PbI3 Solar Cells: Charge Transport, Recombination, and Diffusion Length. *J. Phys. Chem. Lett.* **2014**, *5* (3), 490−494.
(29) Protesescu, L.; Yakunin, S.; Bodnarchuk, M. I.; Krieg, F.; Caputo, R.; Hendon, C. H.; Yang, R. X.; Walsh, A.; Kovalenko, M. V. Nanocrystals of Cesium Lead Halide Perovskites (CsPbX3, X= Cl, Br, and I): Novel Optoelectronic Materials Showing Bright Emission with Wide Color Gamut. *Nano Lett.* **2015**, *15* (6), 3692−3696.
(30) Protesescu, L.; Yakunin, S.; Bodnarchuk, M. I.; Bertolotti, F.; Masciocchi, N.; Guagliardi, A.; Kovalenko, M. V. Monodisperse Formamidinium Lead Bromide Nanocrystals with Bright and Stable Green Photoluminescence. *J. Am. Chem. Soc.* **2016**, *138* (43), 14202−14205.
(31) Rainò, G.; Nedelcu, G.; Protesescu, L.; Bodnarchuk, M. I.; Kovalenko, M. V.; Mahrt, R. F.; Stöferle, T. Single Cesium Lead Halide Perovskite Nanocrystals at Low Temperature: Fast Single-Photon Emission, Reduced Blinking, and Exciton Fine Structure. *ACS Nano* **2016**, *10* (2), 2485−2490.
(32) Mayers, M. Z.; Tan, L. Z.; Egger, D. A.; Rappe, A. M.; Reichman, D. R. How Lattice and Charge Fluctuations Control Carrier Dynamics in Halide Perovskites. *Nano Lett.* **2018**, *18* (12), 8041−8046.
(33) Comin, R.; Crawford, M. K.; Said, A. H.; Herron, N.; Guise, W. E.; Wang, X.; Whitfield, P. S.; Jain, A.; Gong, X.; McGaughey, A. J. H.; et al. Lattice Dynamics and the Nature of Structural Transitions in Organolead Halide Perovskites. *Phys. Rev. B* **2016**, *94* (9), 94301.
(34) Yaffe, O.; Guo, Y.; Tan, L. Z.; Egger, D. A.; Hull, T.; Stoumpos, C. C.; Zheng, F.; Heinz, T. F.; Kronik, L.; Kanatzidis, M. G.; et al. Local Polar Fluctuations in Lead Halide Perovskite Crystals. *Phys. Rev. Lett.* **2017**, *118*, 136001.
(35) Egger, D. A.; Bera, A.; Cahen, D.; Hodes, G.; Kirchartz, T.; Kronik, L.; Lovrincic, R.; Rappe, A. M.; Reichman, D. R.; Yaffe, O. What Remains Unexplained about the Properties of Halide Perovskites? *Adv. Mater.* **2018**, *30*, 1800691.
(36) Yaffe, O.; Guo, Y.; Hull, T.; Stoumpos, C. C.; Tan, L. Z.; Egger, D. A.; Zheng, F.; Szpak, G.; Semonin, O. E.; Beecher, A. N.; et al. The Nature of Dynamic Disorder in Lead Halide Perovskite Crystals. *arXiv:Cond-Mat*, 2016, 1604.08107.
(37) Guo, Y.; Yaffe, O.; Hull, T. D.; Owen, J. S.; Reichman, D. R.; Brus, L. E. Dynamic Emission Stokes Shift and Liquid-like Dielectric Solvation of Band Edge Carriers in Lead-Halide Perovskites. *Nat. Commun.* **2019**, *10*, 1175.
(38) Wright, A. D.; Verdi, C.; Milot, R. L.; Eperon, G. E.; Pérez-Osorio, M. A.; Snaith, H. J.; Giustino, F.; Johnston, M. B.; Herz, L. M. Electron-Phonon Coupling in Hybrid Lead Halide Perovskites. *Nat. Commun.* **2016**, *7*, 11755.
(39) McCall, K. M.; Stoumpos, C. C.; Kostina, S. S.; Kanatzidis, M. G.; Wessels, B. W. Strong Electron-Phonon Coupling and Self-Trapped Excitons in the Defect Halide Perovskites A3M2I9 (A = Cs, Rb; M = Bi, Sb). *Chem. Mater.* **2017**, *29* (9), 4129−4145.
(40) Iaru, C. M.; Geuchies, J. J.; Koenraad, P. M.; Vanmaekelbergh, D.; Silov, A. Y. Strong Carrier-Phonon Coupling in Lead Halide Perovskite Nanocrystals. *ACS Nano* **2017**, *11* (11), 11024−11030.
(41) Miyata, K.; Meggiolaro, D.; Trinh, M. T.; Joshi, P. P.; Mosconi, E.; Jones, S. C.; De Angelis, F.; Zhu, X. Y. Large Polarons in Lead Halide Perovskites. *Sci. Adv.* **2017**, *3* (8), No. e1701217.
(42) Ivanovska, T.; Dionigi, C.; Mosconi, E.; De Angelis, F.; Liscio, F.; Morandi, V.; Ruani, G. Long-Lived Photoinduced Polarons in Organohalide Perovskites. *J. Phys. Chem. Lett.* **2017**, *8* (13), 3081−3086.
(43) Meggiolaro, D.; Ambrosio, F.; Mosconi, E.; Mahata, A.; De Angelis, F. Polarons in Metal Halide Perovskites. *Adv. Energy Mater.* **2020**, *10* (13), 1902748.
(44) Cao, D. H.; Stoumpos, C. C.; Farha, O. K.; Hupp, J. T.; Kanatzidis, M. G. 2D Homologous Perovskites as Light-Absorbing Materials for Solar Cell Applications. *J. Am. Chem. Soc.* **2015**, *137* (24), 7843−7850.
(45) Shamsi, J.; Dang, Z.; Bianchini, P.; Canale, C.; Di Stasio, F.; Brescia, R.; Prato, M.; Manna, L. Colloidal Synthesis of Quantum Confined Single Crystal CsPbBr3 Nanosheets with Lateral Size Control up to the Micrometer Range. *J. Am. Chem. Soc.* **2016**, *138* (23), 7240−7243.
(46) Bekenstein, Y.; Koscher, B. A.; Eaton, S. W.; Yang, P.; Alivisatos, A. P. Highly Luminescent Colloidal Nanoplates of Perovskite Cesium Lead Halide and Their Oriented Assemblies. *J. Am. Chem. Soc.* **2015**, *137* (51), 16008−16011.
(47) Isarov, M.; Tan, L. Z.; Bodnarchuk, M. I.; Kovalenko, M. V.; Rappe, A. M.; Lifshitz, E. Rashba Effect in a Single Colloidal CsPbBr3 Perovskite Nanocrystal Detected by Magneto-Optical Measurements. *Nano Lett.* **2017**, *17* (8), 5020−5026.
(48) Fu, M.; Tamarat, P.; Trebbia, J. B.; Bodnarchuk, M. I.; Kovalenko, M. V.; Even, J.; Lounis, B. Unraveling Exciton-Phonon Coupling in Individual FAPbI3 Nanocrystals Emitting near-Infrared Single Photons. *Nat. Commun.* **2018**, *9*, 3318.
(49) Fu, M.; Tamarat, P.; Huang, H.; Even, J.; Rogach, A. L.; Lounis, B. Neutral and Charged Exciton Fine Structure in Single Lead Halide Perovskite Nanocrystals Revealed by Magneto-Optical Spectroscopy. *Nano Lett.* **2017**, *17* (5), 2895−2901.
(50) Tamarat, P.; Hou, L.; Trebbia, J. B.; Swarnkar, A.; Biadala, L.; Louyer, Y.; Bodnarchuk, M. I.; Kovalenko, M. V.; Even, J.; Lounis, B. The Dark Exciton Ground State Promotes Photon-Pair Emission in Individual Perovskite Nanocrystals. *Nat. Commun.* **2020**, *11*, 6001.
(51) Makarov, N. S.; Guo, S.; Isaienko, O.; Liu, W.; Robel, I.; Klimov, V. I. Spectral and Dynamical Properties of Single Excitons, Biexcitons, and Trions in Cesium-Lead-Halide Perovskite Quantum Dots. *Nano Lett.* **2016**, *16* (4), 2349−2362.
(52) Tilchin, J.; Dirin, D. N.; Maikov, G. I.; Sashchiuk, A.; Kovalenko, M. V.; Lifshitz, E. Hydrogen-Like Wannier-Mott Excitons in Single Crystal of Methylammonium Lead Bromide Perovskite. *ACS Nano* **2016**, *10* (6), 6363−6371.
(53) Rainò, G.; Becker, M. A.; Bodnarchuk, M. I.; Mahrt, R. F.; Kovalenko, M. V.; Stöferle, T. Superfluorescence from Lead Halide Perovskite Quantum Dot Superlattices. *Nature* **2018**, *563* (7733), 671−675.
(54) Eperon, G. E.; Leijtens, T.; Bush, K. A.; Prasanna, R.; Green, T.; Wang, J. T. W.; McMeekin, D. P.; Volonakis, G.; Milot, R. L.; May, R.; et al. Perovskite-Perovskite Tandem Photovoltaics with Optimized Band Gaps. *Science (80-.).* **2016**, *354* (6314), 861−865.
(55) Ashner, M. N.; Shulenberger, K. E.; Krieg, F.; Powers, E. R.; Kovalenko, M. V.; Bawendi, M. G.; Tisdale, W. A. Size-Dependent Biexciton Spectrum in Cspbbr3 Perovskite Nanocrystals. *ACS Energy Lett.* **2019**, *4* (11), 2639−2645.
(56) Hou, L.; Tamarat, P.; Lounis, B. Revealing the Exciton Fine Structure in Lead Halide Perovskite Nanocrystals. *Nanomaterials* **2021**, *11* (4), 1058.
(57) Becker, M. A.; Vaxenburg, R.; Nedelcu, G.; Sercel, P. C.; Shabaev, A.; Mehl, M. J.; Michopoulos, J. G.; Lambrakos, S. G.; Bernstein, N.; Lyons, J. L.; et al. Bright Triplet Excitons in Caesium Lead Halide Perovskites. *Nature* **2018**, *553* (7687), 189−193.
(58) Tamarat, P.; Bodnarchuk, M. I.; Trebbia, J.; Erni, R.; Kovalenko, M. V.; Even, J.; Lounis, B. Lead Bromide Perovskite Nanocrystals Is a Singlet Dark State. *Nat. Mater.* **2019**, *18*, 717−724.
(59) Frohna, K.; Deshpande, T.; Harter, J.; Peng, W.; Barker, B. A.; Neaton, J. B.; Louie, S. G.; Bakr, O. M.; Hsieh, D.; Bernardi, M. Inversion Symmetry and Bulk Rashba Effect in Methylammonium Lead Iodide Perovskite Single Crystals. *Nat. Commun.* **2018**, *9*, 1829.
(60) Zhai, Y.; Baniya, S.; Zhang, C.; Li, J.; Haney, P.; Sheng, C. X.; Ehrenfreund, E.; Vardeny, Z. V. Giant Rashba Splitting in 2D

https://doi.org/10.1021/acs.chemmater.1c03822
Chem. Mater. XXXX, XXX, XXX−XXX

Organic-Inorganic Halide Perovskites Measured by Transient Spectroscopies. *Sci. Adv.* **2017**, *3* (7), No. e1700704.
(61) Liu, X.; Chanana, A.; Huynh, U.; Xue, F.; Haney, P.; Blair, S.; Jiang, X.; Vardeny, Z. V. Circular Photogalvanic Spectroscopy of Rashba Splitting in 2D Hybrid Organic-Inorganic Perovskite Multiple Quantum Wells. *Nat. Commun.* **2020**, *11*, 323.
(62) Sercel, P. C.; Vardeny, Z. V.; Efros, A. L. Circular Dichroism in Non-Chiral Metal Halide Perovskites. *Nanoscale* **2020**, *12* (35), 18067−18078.
(63) Etienne, T.; Mosconi, E.; De Angelis, F. Dynamical Origin of the Rashba Effect in Organohalide Lead Perovskites: A Key to Suppressed Carrier Recombination in Perovskite Solar Cells? *J. Phys. Chem. Lett.* **2016**, *7* (9), 1638−1645.
(64) Meggiolaro, D.; Mosconi, E.; De Angelis, F. Formation of Surface Defects Dominates Ion Migration in Lead-Halide Perovskites. *ACS Energy Lett.* **2019**, *4* (3), 779−785.
(65) Zheng, F.; Tan, L. Z.; Liu, S.; Rappe, A. M. Rashba Spin-Orbit Coupling Enhanced Carrier Lifetime in CH 3 NH 3 PbI 3. *Nano Lett.* **2015**, *15* (12), 7794−7800.
(66) Kepenekian, M.; Even, J. Rashba and Dresselhaus Couplings in Halide Perovskites: Accomplishments and Opportunities for Spintronics and Spin-Orbitronics. *J. Phys. Chem. Lett.* **2017**, *8* (14), 3362−3370.
(67) Kepenekian, M.; Robles, R.; Katan, C.; Sapori, D.; Pedesseau, L.; Even, J. Rashba and Dresselhaus Effects in Hybrid Organic-Inorganic Perovskites: From Basics to Devices. *ACS Nano* **2015**, *9* (12), 11557−11567.
(68) Even, J.; Pedesseau, L.; Katan, C. Understanding Quantum Confinement of Charge Carriers in Layered 2D Hybrid Perovskites. *ChemPhysChem* **2014**, *15* (17), 3733−3741.
(69) Giovanni, D.; Ma, H.; Chua, J.; Grätzel, M.; Ramesh, R.; Mhaisalkar, S.; Mathews, N.; Sum, T. C. Highly Spin-Polarized Carrier Dynamics and Ultralarge Photoinduced Magnetization in CH3NH3PbI3 Perovskite Thin Films. *Nano Lett.* **2015**, *15* (3), 1553−1558.
(70) Niesner, D.; Hauck, M.; Shrestha, S.; Levchuk, I.; Matt, G. J.; Osvet, A.; Batentschuk, M.; Brabec, C.; Weber, H. B.; Fauster, T. Structural Fluctuations Cause Spin-Split States in Tetragonal (CH3NH3)PbI3 as Evidenced by the Circular Photogalvanic Effect. *Proc. Natl. Acad. Sci. Acad. Sci.* **2018**, *115*, 9509−9514.
(71) Becker, M. A.; Bernasconi, C.; Bodnarchuk, M. I.; Raino, G.; Kovalenko, M. V.; Norris, D. J.; Mahrt, R. F.; Stoferle, T. Unraveling the Origin of the Long Fluorescence Decay Component of Cesium Lead Halide Perovskite Nanocrystals. *ACS Nano* **2020**, *14* (11), 14939−14946.
(72) Zhang, C.; Sun, D.; Sheng, C. X.; Zhai, Y. X.; Mielczarek, K.; Zakhidov, A.; Vardeny, Z. V. Magnetic Field Effects in Hybrid Perovskite Devices. *Nat. Phys.* **2015**, *11* (5), 427−434.
(73) Wang, J.; Zhang, C.; Liu, H.; McLaughlin, R.; Zhai, Y.; Vardeny, S. R.; Liu, X.; McGill, S.; Semenov, D.; Guo, H.; et al. Spin-Optoelectronic Devices Based on Hybrid Organic-Inorganic Trihalide Perovskites. *Nat. Commun.* **2019**, *10*, 129.
(74) Odenthal, P.; Talmadge, W.; Gundlach, N.; Wang, R.; Zhang, C.; Sun, D.; Yu, Z. G.; Valy Vardeny, Z.; Li, Y. S. Spin-Polarized Exciton Quantum Beating in Hybrid Organic-Inorganic Perovskites. *Nat. Phys.* **2017**, *13* (9), 894−899.
(75) Belykh, V. V.; Yakovlev, D. R.; Glazov, M. M.; Grigoryev, P. S.; Hussain, M.; Rautert, J.; Dirin, D. N.; Kovalenko, M. V.; Bayer, M. Coherent Spin Dynamics of Electrons and Holes in CsPbBr3 Perovskite Crystals. *Nat. Commun.* **2019**, *10*, 673.
(76) Utzat, H.; Sun, W.; Kaplan, A. E. K.; Krieg, F.; Ginterseder, M.; Spokoyny, B.; Klein, N. D.; Shulenberger, K. E.; Perkinson, C. F.; Kovalenko, M. V.; et al. Coherent Single-Photon Emission from Colloidal Lead Halide Perovskite Quantum Dots. *Science (80-.).* **2019**, *363*, 1068−1072.
(77) Crane, M. J.; Jacoby, L. M.; Cohen, T. A.; Huang, Y.; Luscombe, C. K.; Gamelin, D. R. Coherent Spin Precession and Lifetime-Limited Spin Dephasing in CsPbBr3 Perovskite Nanocrystals. *Nano Lett.* **2020**, *20* (12), 8626−8633.
(78) Chen, X.; Lu, H.; Li, Z.; Zhai, Y.; Ndione, P. F.; Berry, J. J.; Zhu, K.; Yang, Y.; Beard, M. C. Impact of Layer Thickness on the Charge Carrier and Spin Coherence Lifetime in Two-Dimensional Layered Perovskite Single Crystals. *ACS Energy Lett.* **2018**, *3* (9), 2273−2279.
(79) Chekhovich, E. A.; Hopkinson, M.; Skolnick, M. S.; Tartakovskii, A. I. Suppression of Nuclear Spin Bath Fluctuations in Self-Assembled Quantum Dots Induced by Inhomogeneous Strain. *Nat. Commun.* **2015**, *6*, 6348.
(80) Warburton, R. J. Single Spins in Self-Assembled Quantum Dots. *Nat. Mater.* **2013**, *12* (6), 483−493.
(81) Chen, T.; Chen, W.-L.; Foley, B. J.; Lee, J.; Ruff, J. P. C.; Ko, J. Y. P.; Brown, C. M.; Harriger, L. W.; Zhang, D.; Park, C.; et al. Origin of Long Lifetime of Band-Edge Charge Carriers in Organic-Inorganic Lead Iodide Perovskites. *Proc. Natl. Acad. Sci. U. S. A.* **2017**, *114* (29), 7519−7524.
(82) Becker, M. A.; Scarpelli, L.; Nedelcu, G.; Rainò, G.; Masia, F.; Borri, P.; Stöferle, T.; Kovalenko, M. V.; Langbein, W.; Mahrt, R. F. Long Exciton Dephasing Time and Coherent Phonon Coupling in CsPbBr 2 Cl Perovskite Nanocrystals. *Nano Lett.* **2018**, *18* (12), 7546−7551.
(83) Rainò, G.; Utzat, H.; Bawendi, M. G.; Kovalenko, M. V. Superradiant Emission from Self-Assembled Light Emitters: From Molecules to Quantum Dots. *MRS Bull.* **2020**, *45* (10), 841−848.
(84) Cherniukh, I.; Rainò, G.; Stöferle, T.; Burian, M.; Travesset, A.; Naumenko, D.; Amenitsch, H.; Erni, R.; Mahrt, R. F.; Bodnarchuk, M. I.; et al. Perovskite-Type Superlattices from Lead Halide Perovskite Nanocubes. *Nature* **2021**, *593* (7860), 535−542.
(85) Yu, Z. G. Effective-Mass Model and Magneto-Optical Properties in Hybrid Perovskites. *Sci. Rep.* **2016**, *6*, 28576.
(86) Chen, Z.; Dong, G.; Qiu, J. Ultrafast Pump-Probe Spectroscopy—A Powerful Tool for Tracking Spin-Quantum Dynamics in Metal Halide Perovskites. *Adv. Quantum Technol.* **2021**, *4*, 2100052.
(87) Parobek, D.; Dong, Y.; Qiao, T.; Son, D. H. Direct Hot-Injection Synthesis of Mn-Doped CsPbBr3 Nanocrystals. *Chem. Mater.* **2018**, *30* (9), 2939−2944.
(88) Dey, A.; Ye, J.; De, A.; Debroye, E.; Ha, S. K.; Bladt, E.; Kshirsagar, A. S.; Wang, Z.; Yin, J.; Wang, Y.; et al. State of the Art and Prospects for Halide Perovskite Nanocrystals. *ACS Nano* **2021**, *15* (7), 10775−10981.
(89) Luo, B.; Li, F.; Xu, K.; Guo, Y.; Liu, Y.; Xia, Z.; Zhang, J. Z. B-Site Doped Lead Halide Perovskites: Synthesis, Band Engineering, Photophysics, and Light Emission Applications. *J. Mater. Chem. C* **2019**, *7* (10), 2781−2808.
(90) Sarkar, P.; Srivastava, A.; Tripathy, S. K.; Baishnab, K. L.; Lenka, T. R.; Menon, P. S.; Lin, F.; Aberle, A. G. Impact of Sn Doping on Methylammonium Lead Chloride Perovskite: An Experimental Study. *J. Appl. Phys.* **2020**, *127*, 125110.
(91) Jellicoe, T. C.; Richter, J. M.; Glass, H. F. J.; Tabachnyk, M.; Brady, R.; Dutton, S. E.; Rao, A.; Friend, R. H.; Credgington, D.; Greenham, N. C.; et al. Synthesis and Optical Properties of Lead-Free Cesium Tin Halide Perovskite Nanocrystals. *J. Am. Chem. Soc.* **2016**, *138* (9), 2941−2944.
(92) Chen, L. J.; Lee, C. R.; Chuang, Y. J.; Wu, Z. H.; Chen, C. Synthesis and Optical Properties of Lead-Free Cesium Tin Halide Perovskite Quantum Rods with High-Performance Solar Cell Application. *J. Phys. Chem. Lett.* **2016**, *7* (24), 5028−5035.
(93) Feng, J.; Xiao, B. Effective Masses and Electronic and Optical Properties of Nontoxic MASnX3 (X = Cl, Br, and I) Perovskite Structures as Solar Cell Absorber: A Theoretical Study Using HSE06. *J. Phys. Chem. C* **2014**, *118* (34), 19655−19660.
(94) Pradhan, B.; Kumar, G. S.; Sain, S.; Dalui, A.; Ghorai, U. K.; Pradhan, S. K.; Acharya, S. Size Tunable Cesium Antimony Chloride Perovskite Nanowires and Nanorods. *Chem. Mater.* **2018**, *30* (6), 2135−2142.
(95) Pal, J.; Bhunia, A.; Chakraborty, S.; Manna, S.; Das, S.; Dewan, A.; Datta, S.; Nag, A. Synthesis and Optical Properties of Colloidal M3Bi2I9 (M = Cs, Rb) Perovskite Nanocrystals. *J. Phys. Chem. C* **2018**, *122* (19), 10643−10649.

https://doi.org/10.1021/acs.chemmater.1c03822
Chem. Mater. XXXX, XXX, XXX−XXX

(96) Park, B. W.; Philippe, B.; Zhang, X.; Rensmo, H.; Boschloo, G.; Johansson, E. M. J. Bismuth Based Hybrid Perovskites A3Bi2I9 (A: Methylammonium or Cesium) for Solar Cell Application. *Adv. Mater.* **2015**, *27* (43), 6806−6813.
(97) Nelson, R. D.; Santra, K.; Wang, Y.; Hadi, A.; Petrich, J. W.; Panthani, M. G. Synthesis and Optical Properties of Ordered-Vacancy Perovskite Cesium Bismuth Halide Nanocrystals. *Chem. Commun.* **2018**, *54* (29), 3640−3643.
(98) Bi, C.; Wang, S.; Li, Q.; Kershaw, S. V.; Tian, J.; Rogach, A. L. Thermally Stable Copper(II)-Doped Cesium Lead Halide Perovskite Quantum Dots with Strong Blue Emission. *J. Phys. Chem. Lett.* **2019**, *10* (5), 943−952.
(99) Zhou, S.; Zhu, Y.; Zhong, J.; Tian, F.; Huang, H.; Chen, J.; Chen, D. Chlorine-Additive-Promoted Incorporation of Mn2+ Dopants into CsPbCl3 Perovskite Nanocrystals. *Nanoscale* **2019**, *11* (26), 12465−12470.
(100) Kubicki, D. J.; Prochowicz, D.; Pinon, A.; Stevanato, G.; Hofstetter, A.; Zakeeruddin, S. M.; Grätzel, M.; Emsley, L. Doping and Phase Segregation in Mn 2+ - and Co 2+ -Doped Lead Halide Perovskites from 133 Cs and 1 H NMR Relaxation Enhancement. *J. Mater. Chem. A* **2019**, *7* (5), 2326−2333.
(101) Ahmed, G. H.; Yin, J.; Bakr, O. M.; Mohammed, O. F. Near-Unity Photoluminescence Quantum Yield in Inorganic Perovskite Nanocrystals by Metal-Ion Doping. *J. Chem. Phys.* **2020**, *152*, 020902.
(102) Yong, Z. J.; Guo, S. Q.; Ma, J. P.; Zhang, J. Y.; Li, Z. Y.; Chen, Y. M.; Zhang, B. B.; Zhou, Y.; Shu, J.; Gu, J. L.; et al. Doping-Enhanced Short-Range Order of Perovskite Nanocrystals for Near-Unity Violet Luminescence Quantum Yield. *J. Am. Chem. Soc.* **2018**, *140* (31), 9942−9951.
(103) Behera, R. K.; Dutta, A.; Ghosh, D.; Bera, S.; Bhattacharyya, S.; Pradhan, N. Doping the Smallest Shannon Radii Transition Metal Ion Ni(II) for Stabilizing α-CsPbI3 Perovskite Nanocrystals. *J. Phys. Chem. Lett.* **2019**, *10* (24), 7916−7921.
(104) Xing, K.; Yuan, X.; Wang, Y.; Li, J.; Wang, Y.; Fan, Y.; Yuan, L.; Li, K.; Wu, Z.; Li, H.; et al. Improved Doping and Emission Efficiencies of Mn-Doped CsPbCl3 Perovskite Nanocrystals via Nickel Chloride. *J. Phys. Chem. Lett.* **2019**, *10* (15), 4177−4184.
(105) Liu, M.; Jiang, N.; Huang, H.; Lin, J.; Huang, F.; Zheng, Y.; Chen, D. Ni2+-Doped CsPbI3 Perovskite Nanocrystals with near-Unity Photoluminescence Quantum Yield and Superior Structure Stability for Red Light-Emitting Devices. *Chem. Eng. J.* **2021**, *413*, 127547.
(106) Thawarkar, S.; Rana, P. J. S.; Narayan, R.; Singh, S. P. Ni-Doped CsPbBr3 Perovskite: Synthesis of Highly Stable Nanocubes. *Langmuir* **2019**, *35* (52), 17150−17155.
(107) Islam, M. N.; Hadi, M. A.; Podder, J. Influence of Ni Doping in a Lead-Halide and a Lead-Free Halide Perovskites for Optoelectronic Applications. *AIP Adv.* **2019**, *9*, 125321.
(108) Ketavath, R.; Katturi, N. K.; Ghugal, S. G.; Kolli, H. K.; Swetha, T.; Soma, V. R.; Murali, B. Deciphering the Ultrafast Nonlinear Optical Properties and Dynamics of Pristine and Ni-Doped CsPbBr3 Colloidal Two-Dimensional Nanocrystals. *J. Phys. Chem. Lett.* **2019**, *10* (18), 5577−5584.
(109) Zhang, R.; Yuan, Y.; Zhang, J.; Liu, H.; Chen, G.; Li, K.; Hong, M. Q.; Zuo, W.; Wang, C.; Yang, W.; et al. Improving the Mn2+ Emission and Stability of CsPb(Cl/Br)3 Nanocrystals by Ni2+ Doping in Ambient Air. *J. Mater. Sci.* **2021**, *56* (12), 7494−7507.
(110) Su, B.; Zhou, G.; Huang, J.; Song, E.; Nag, A.; Xia, Z. Mn2+-Doped Metal Halide Perovskites: Structure, Photoluminescence, and Application. *Laser Photonics Rev.* **2021**, *15* (1), 2000334.
(111) Shapiro, A.; Heindl, M. W.; Horani, F.; Dahan, M. H.; Tang, J.; Amouyal, Y.; Lifshitz, E. Significance of Ni Doping in CsPbX3 Nanocrystals via Postsynthesis Cation-Anion Coexchange. *J. Phys. Chem. C* **2019**, *123* (40), 24979−24987.
(112) Xu, K.; Lin, C. C.; Xie, X.; Meijerink, A. Efficient and Stable Luminescence from Mn2+ in Core and Core-Isocrystalline Shell CsPbCl3 Perovskite Nanocrystals. *Chem. Mater.* **2017**, *29* (10), 4265−4272.
(113) Mir, W. J.; Jagadeeswararao, M.; Das, S.; Nag, A. Colloidal Mn-Doped Cesium Lead Halide Perovskite Nanoplatelets. *ACS Energy Lett.* **2017**, *2* (3), 537−543.
(114) Guria, A. K.; Dutta, S. K.; Adhikari, S. D.; Pradhan, N. Doping Mn2+ in Lead Halide Perovskite Nanocrystals: Successes and Challenges. *ACS Energy Lett.* **2017**, *2* (5), 1014−1021.
(115) Huang, G.; Wang, C.; Xu, S.; Zong, S.; Lu, J.; Wang, Z.; Lu, C.; Cui, Y. Postsynthetic Doping of MnCl2Molecules into Preformed CsPbBr3 Perovskite Nanocrystals via a Halide Exchange-Driven Cation Exchange. *Adv. Mater.* **2017**, *29* (29), 1700095.
(116) Li, F.; Xia, Z.; Gong, Y.; Gu, L.; Liu, Q. Optical Properties of Mn2+ Doped Cesium Lead Halide Perovskite Nanocrystals: Via a Cation-Anion Co-Substitution Exchange Reaction. *J. Mater. Chem. C* **2017**, *5* (36), 9281−9287.
(117) Parobek, D.; Roman, B. J.; Dong, Y.; Jin, H.; Lee, E.; Sheldon, M.; Son, D. H. Exciton-to-Dopant Energy Transfer in Mn-Doped Cesium Lead Halide Perovskite Nanocrystals. *Nano Lett.* **2016**, *16* (12), 7376−7380.
(118) Chen, D.; Zhou, S.; Fang, G.; Chen, X.; Zhong, J. Fast Room-Temperature Cation Exchange Synthesis of Mn-Doped CsPbCl3 Nanocrystals Driven by Dynamic Halogen Exchange. *ACS Appl. Mater. Interfaces* **2018**, *10* (46), 39872−39878.
(119) Zhang, K.; Zhao, J.; Hu, Q.; Yang, S.; Zhu, X.; Zhang, Y.; Huang, R.; Ma, Y.; Wang, Z.; Ouyang, Z.; et al. Room-Temperature Magnetic Field Effect on Excitonic Photoluminescence in Perovskite Nanocrystals. *Adv. Mater.* **2021**, *33*, 2008225.
(120) Neumann, T.; Feldmann, S.; Moser, P.; Delhomme, A.; Zerhoch, J.; van de Goor, T.; Wang, S.; Dyksik, M.; Winkler, T.; Finley, J. J.; et al. Manganese Doping for Enhanced Magnetic Brightening and Circular Polarization Control of Dark Excitons in Paramagnetic Layered Hybrid Metal-Halide Perovskites. *Nat. Commun.* **2021**, *12*, 3489.
(121) Xu, K.; Vliem, J. F.; Meijerink, A. Long-Lived Dark Exciton Emission in Mn-Doped CsPbCl 3 Perovskite Nanocrystals. *J. Phys. Chem. C* **2019**, *123*, 979−984.
(122) Chen, Z.; Chen, H.; Zhang, C.; Chen, L.; Qin, Z.; Sang, H.; Wang, X.; Xiao, M. Excitation-Tailored Dual-Color Emission of Manganese(II)-Doped Perovskite Nanocrystals. *Appl. Phys. Lett.* **2019**, *114*, 041902.
(123) Wang, F.; Gao, H.; de Graaf, C.; Poblet, J. M.; Campbell, B. J.; Stroppa, A. Switchable Rashba Anisotropy in Layered Hybrid Organic-Inorganic Perovskite by Hybrid Improper Ferroelectricity. *npj Comput. Mater.* **2020**, *6*, 183.
(124) Zheng, X.; Hou, Y.; Sun, H. T.; Mohammed, O. F.; Sargent, E. H.; Bakr, O. M. Reducing Defects in Halide Perovskite Nanocrystals for Light-Emitting Applications. *J. Phys. Chem. Lett.* **2019**, *10* (10), 2629−2640.
(125) Leng, M.; Yang, Y.; Chen, Z.; Gao, W.; Zhang, J.; Niu, G.; Li, D.; Song, H.; Zhang, J.; Jin, S.; et al. Surface Passivation of Bismuth-Based Perovskite Variant Quantum Dots to Achieve Efficient Blue Emission. *Nano Lett.* **2018**, *18* (9), 6076−6083.
(126) Milstein, T. J.; Kluherz, K. T.; Kroupa, D. M.; Erickson, C. S.; De Yoreo, J. J.; Gamelin, D. R. Anion Exchange and the Quantum-Cutting Energy Threshold in Ytterbium-Doped CsPb(Cl 1- x Br x) 3 Perovskite Nanocrystals. *Nano Lett.* **2019**, *19* (3), 1931−1937.
(127) Zhou, D.; Liu, D.; Pan, G.; Chen, X.; Li, D.; Xu, W.; Bai, X.; Song, H. Cerium and Ytterbium Codoped Halide Perovskite Quantum Dots: A Novel and Efficient Downconverter for Improving the Performance of Silicon Solar Cells. *Adv. Mater.* **2017**, *29*, 1704149.
(128) Zhang, C.; Zhang, A.; Liu, T.; Zhou, L.; Zheng, J.; Zuo, Y.; He, Y.; Li, J. A Facile Method for Preparing Yb3+-Doped Perovskite Nanocrystals with Ultra-Stable near-Infrared Light Emission. *RSC Adv.* **2020**, *10* (30), 17635−17641.
(129) Mir, W. J.; Mahor, Y.; Lohar, A.; Jagadeeswararao, M.; Das, S.; Mahamuni, S.; Nag, A. Postsynthesis Doping of Mn and Yb into CsPbX3 (X = Cl, Br, or I) Perovskite Nanocrystals for Down-conversion Emission. *Chem. Mater.* **2018**, *30* (22), 8170−8178.

https://doi.org/10.1021/acs.chemmater.1c03822
Chem. Mater. XXXX, XXX, XXX−XXX

(130) Zhang, X.; Zhang, Y.; Zhang, X.; Yin, W.; Wang, Y.; Wang, H.; Lu, M.; Li, Z.; Gu, Z.; Yu, W. W. Yb3+ and Yb3+/Er3+ Doping for near-Infrared Emission and Improved Stability of CsPbCl3 Nanocrystals. *J. Mater. Chem. C* **2018**, *6* (37), 10101−10105.
(131) Pan, G.; Bai, X.; Yang, D.; Chen, X.; Jing, P.; Qu, S.; Zhang, L.; Zhou, D.; Zhu, J.; Xu, W.; et al. Doping Lanthanide into Perovskite Nanocrystals: Highly Improved and Expanded Optical Properties. *Nano Lett.* **2017**, *17* (12), 8005−8011.
(132) Kroupa, D. M.; Roh, J. Y.; Milstein, T. J.; Creutz, S. E.; Gamelin, D. R. Quantum-Cutting Ytterbium-Doped CsPb(Cl1-XBrx)3 Perovskite Thin Films with Photoluminescence Quantum Yields over 190%. *ACS Energy Lett.* **2018**, *3* (10), 2390−2395.
(133) Milstein, T. J.; Kroupa, D. M.; Gamelin, D. R. Picosecond Quantum Cutting Generates Photoluminescence Quantum Yields over 100% in Ytterbium-Doped CsPbCl3 Nanocrystals. *Nano Lett.* **2018**, *18* (6), 3792−3799.
(134) Liu, Y.; Chen, W.; Zhong, J.; Chen, D. Upconversion Luminescence in Yb/Ln (Ln = Er, Tm) Doped Oxyhalide Glasses Containing CsPbBr3 Perovskite Nanocrystals. *J. Eur. Ceram. Soc.* **2019**, *39* (14), 4275−4282.
(135) Mir, W. J.; Sheikh, T.; Arfin, H.; Xia, Z.; Nag, A. Lanthanide Doping in Metal Halide Perovskite Nanocrystals: Spectral Shifting, Quantum Cutting and Optoelectronic Applications. *NPG Asia Mater.* **2020**, *12*, 9.
(136) Zeng, M.; Locardi, F.; Mara, D.; Hens, Z.; Van Deun, R.; Artizzu, F. Switching on Near-Infrared Light in Lanthanide-Doped CsPbCl3perovskite Nanocrystals. *Nanoscale* **2021**, *13* (17), 8118−8125.
(137) Wang, H. Q.; Kuang, X. Y.; Li, H. F. Studies of EPR Theory and Trigonal Distortion of the (NiX6)4- Clusters (X = Halide Ion) in the Series of Perovskite Crystals AMX3 (A = Rb, Cs; M = Cd, Mg; X = Halide Ion). *Chem. Phys. Lett.* **2008**, *460*, 365−369.
(138) McPherson, G. L.; Koch, R. C.; Stucky, G. D. Electron Spin Resonance Spectra of V2+, Mn2+, and Ni2+ in Single Crystals of CsMgBr3 and CsMgI3. *J. Chem. Phys.* **1974**, *60*, 1424.
(139) Lee, S. M.; Moon, C. J.; Lim, H.; Lee, Y.; Choi, M. Y.; Bang, J. Temperature-Dependent Photoluminescence of Cesium Lead Halide Perovskite Quantum Dots: Splitting of the Photoluminescence Peaks of CsPbBr3 and CsPb(Br/I)3 Quantum Dots at Low Temperature. *J. Phys. Chem. C* **2017**, *121* (46), 26054−26062.
(140) Diroll, B. T.; Nedelcu, G.; Kovalenko, M. V.; Schaller, R. D. High-Temperature Photoluminescence of CsPbX3 (X = Cl, Br, I) Nanocrystals. *Adv. Funct. Mater.* **2017**, *27*, 1606750.
(141) Shinde, A.; Gahlaut, R.; Mahamuni, S. Low-Temperature Photoluminescence Studies of CsPbBr3 Quantum Dots. *J. Phys. Chem. C* **2017**, *121* (27), 14872−14878.
(142) Yuan, X.; Jing, P.; Li, J.; Wei, M.; Hua, J.; Zhao, J.; Tian, L.; Li, J. Temperature-Dependent Photoluminescence of Inorganic Perovskite Nanocrystal Films. *RSC Adv.* **2016**, *6* (82), 78311−78316.
(143) Canneson, D.; Shornikova, E. V.; Yakovlev, D. R.; Rogge, T.; Mitioglu, A. A.; Ballottin, M. V.; Christianen, P. C. M.; Lhuillier, E.; Bayer, M.; Biadala, L. Negatively Charged and Dark Excitons in CsPbBr3 Perovskite Nanocrystals Revealed by High Magnetic Fields. *Nano Lett.* **2017**, *17* (10), 6177−6183.
(144) Lifshitz, E.; Dehnel, J.; Barak, Y.; Meir, I.; Budniak, A. K.; Nagvenkar, A. P.; Gamelin, D. R. Insight into the Spin Properties in Undoped and Mn-Doped CdSe/CdS-Seeded Nanorods by Optically Detected Magnetic Resonance. *ACS Nano* **2020**, *14* (10), 13478−13490.
(145) Lifshitz, E.; Fradkin, L.; Glozman, A.; Langof, L. Optically Detected Magnetic Resonance Studies of Colloidal Semiconductor Nanocrystals. *Annu. Rev. Phys. Chem.* **2004**, *55* (1), 509−557.
(146) Archer, P. I.; Santangelo, S. A.; Gamelin, D. R. Direct Observation of Sp-d Exchange Interactions in Colloidal Mn2+ - And Co2+ -Doped CdSe Quantum Dots. *Nano Lett.* **2007**, *7* (4), 1037−1043.
(147) Beaulac, R.; Feng, Y.; May, J. W.; Badaeva, E.; Gamelin, D. R.; Li, X. Orbital Pathways for Mn2+-Carrier Sp-d Exchange in Diluted Magnetic Semiconductor Quantum Dots. *Phys. Rev. B - Condens. Matter Mater. Phys.* **2011**, *84*, 195324.
(148) Boyer-Richard, S.; Katan, C.; Traoré, B.; Scholz, R.; Jancu, J. M.; Even, J. Symmetry-Based Tight Binding Modeling of Halide Perovskite Semiconductors. *J. Phys. Chem. Lett.* **2016**, *7* (19), 3833−3840.
(149) Sercel, P. C.; Lyons, J. L.; Bernstein, N.; Efros, A. L. Quasicubic Model for Metal Halide Perovskite Nanocrystals. *J. Chem. Phys.* **2019**, *151*, 234106.
(150) Strassberg, R.; Delikanli, S.; Barak, Y.; Dehnel, J.; Kostadinov, A.; Maikov, G.; Hernandez-Martinez, P. L.; Sharma, M.; Demir, H. V.; Lifshitz, E. Persuasive Evidence for Electron-Nuclear Coupling in Diluted Magnetic Colloidal Nanoplatelets Using Optically Detected Magnetic Resonance Spectroscopy. *J. Phys. Chem. Lett.* **2019**, *10* (15), 4437−4447.
(151) Ambrosio, F.; Mosconi, E.; Alasmari, A. A.; Alasmary, F. A. S.; Meggiolaro, D.; De Angelis, F. Formation of Color Centers in Lead Iodide Perovskites: Self-Trapping and Defects in the Bulk and Surfaces. *Chem. Mater.* **2020**, *32* (16), 6916−6924.
(152) Zhang, L.; Hao, Y.; Wu, Y.; Qin, W.; Liu, X.; Cui, B.; Xie, S. Self-Trapping Effect on the Excitonic and Polaronic Properties of a Single-Layer 2D Metal-Halide Perovskite. *2D Mater.* **2020**, *7*, 035020.
(153) Wu, B.; Ning, W.; Xu, Q.; Manjappa, M.; Feng, M.; Ye, S.; Fu, J.; Lie, S.; Yin, T.; Wang, F.; et al. Strong Self-Trapping by Deformation Potential Limits Photovoltaic Performance in Bismuth Double Perovskite. *Sci. Adv.* **2021**, *7*, No. eabd3160.
(154) Gautier, R.; Paris, M.; Massuyeau, F. Exciton Self-Trapping in Hybrid Lead Halides: Role of Halogen. *J. Am. Chem. Soc.* **2019**, *141* (32), 12619−12623.
(155) Li, J.; Wang, H.; Li, D. *Self-Trapped Excitons in Two-Dimensional Perovskites.* **2020**, *13* (3), 225−234.
(156) Wang, S.; Leng, J.; Yin, Y.; Liu, J.; Wu, K.; Jin, S. Ultrafast Dopant-Induced Exciton Auger-like Recombination in Mn-Doped Perovskite Nanocrystals. *ACS Energy Lett.* **2020**, *5*, 328−334.
(157) Zheng, X.; Yuan, S.; Liu, J.; Yin, J.; Yuan, F.; Shen, W. S.; Yao, K.; Wei, M.; Zhou, C.; Song, K.; et al. Chlorine Vacancy Passivation in Mixed Halide Perovskite Quantum Dots by Organic Pseudohalides Enables Efficient Rec. 2020 Blue Light-Emitting Diodes. *ACS Energy Lett.* **2020**, *5* (3), 793−798.
(158) Orton, J. W.; Auzins, P.; Wertz, J. E. Estimate of the Nuclear Moment of Ni61 from Electron Spin Resonance. *Phy. Rev.* **1960**, *119*, 1691.

https://doi.org/10.1021/acs.chemmater.1c03822
Chem. Mater. XXXX, XXX, XXX−XXX